SAND REPORT

SAND2003-1868
Unlimited Release
Printed June 2003

Reflectance-Correcting Pyrometry in Thin FIlm Deposition Applications

W. G. Breiland

Prepared by
Sandia National Laboratories
Albuquerque, New Mexico 87185 and Livermore, California 94550

Sandia is a multiprogram laboratory operated by Sandia Corporation, a Lockheed Martin Company, for the United States Department of Energy under Contract DE-AC04-94AL85000.

Issued by Sandia National Laboratories, operated for the United States Department of Energy by Sandia Corporation.

Available to DOE and DOE contractors from
U.S. Department of Energy
Office of Scientific and Technical Information
P.O. Box 62
Oak Ridge, TN 37831

Telephone: (865)576-8401
Facsimile: (865)576-5728
E-Mail: reports@adonis.osti.gov
Online ordering: http://www.doe.gov/bridge

Available to the public from
U.S. Department of Commerce
National Technical Information Service
5285 Port Royal Rd
Springfield, VA 22161

Telephone: (800)553-6847
Facsimile: (703)605-6900
E-Mail: orders@ntis.fedworld.gov
Online order: http://www.ntis.gov/ordering.htm

SAND2003-1868
Unlimited Release
Printed June 2003

Reflectance-Correcting Pyrometry in Thin Film Deposition Applications

William G. Breiland
Chemical Processing Science Department
Sandia National Laboratories
Albuquerque, NM 87185
Contact: W. G. Breiland, 505-844-7029, wgbreil@sandia.gov

Abstract

A detailed study of an emissivity-correcting pyrometer instrument for measuring wafer surface temperatures during thin film growth is presented. The basic physics is reviewed and preliminary data showing a temperature over-compensation artifact is shown. The rest of the report presents an exhaustive analysis of the potential sources for the temperature over-compensation effect. This analysis yields an *in situ* calibration method that can be used to remove temperature over-compensation artifacts that arise from any first-order systematic error in either the reflectance or thermal emission measurement. With corrections applied, artifact-free surface temperatures can be measured with a precision of a few °C over a wide range of wafer emissivities.

The work in this report resulted in United States Patent US 6,398,406 B1, awarded 4 Jun 2002.

Reflectance-Correcting Pyrometry in Thin Film Deposition Applications

William G. Breiland
wgbreil@sandia.gov

Sandia National Laboratories

Participants in this study:

William G. Breiland
Larry A. Bruskas
Andrew A. Allerman
Terry W. Hargett

Table of Contents

Using This Document

This document comes as an Adobe® Acrobat® 4.0 ".pdf" file, and can be viewed with any computer operating system using "Acrobat Reader", which is available for free from the website: http://www.adobe.com/prodindex/acrobat/readstep.html#reader. Online viewing allows one to take advantage of the bookmarks and links imbedded within the text to quickly jump back and forth to various sections simply by clicking on the bookmark or link. Links are indicated by a dashed blue box surrounding text. Equations are also often linked when mentioned in the text. This allows one to jump to the equation to see the expression, then use the "go back" command to return. Web page links within the document are active, allowing the system to direct a browser to the web page listed in the Acrobat document. A printed copy of the document may be obtained with the "print" command within the Acrobat Reader. Various "Views" are available within the reader to make online reading easier. The hierarchical arrangement of bookmark headings that appears on the left hand side of the document may be toggled on and off with the "show/hide navigation pane" icon on the taskbar. The user also has access to the full text search capabilities of Acrobat Reader.

Introduction

Temperature is a critical factor in the growth of thin films by either chemical vapor deposition (CVD) or molecular beam epitaxy (MBE). It is particularly important in metal-organic CVD (MOCVD) thin film growth because one is often challenged to grow compound semiconductors with a very specific stoichiometry in order to maintain stringent lattice-matching conditions. The chemical reactions responsible for this CVD growth and reactions responsible for doping are in some cases highly temperature dependent. Control of the deposition temperature thus becomes critical. Unfortunately, such control is difficult to achieve. The CVD environment employs reactive and toxic chemicals at high temperatures and requires the utmost in cleanliness to avoid unintentional doping or parasitic chemical reactions. Physical probes of the surface temperature cannot be used in such an environment. Classical optical pyrometry, which measures the thermal emission from the hot semiconductor surface is a strong candidate for a remote, *in situ* temperature probe. However, as thin semiconductor films are deposited, the emissivity of the surface changes dramatically due to optical interference effects between film interfaces. The emissivity change has two consequences. First, the heat loss from the surface of the wafer due to thermal emission is changed by the presence of the thin film. This alters the balance in heat transfer and causes the surface temperature to change as the thin film growth is taking place. Second, a pyrometer that does not account for the emissivity changes will yield grossly inaccurate values for the surface temperature. It is not uncommon to encounter errors as large as 50 °C. To avoid these errors, emissivity changes must be measured and appropriate corrections made to extract an accurate surface temperature.

This report describes the use of fundamental theoretical and experimental methods to develop a robust and accurate emissivity-correcting pyrometer for *in situ* measurement of surface temperature during thin film growth. The use of emissivity-correcting methods in pyrometry is well-documented. It was thus felt at the beginning of the project that this method would yield a relatively straightforward solution to the problem of surface temperature measurement under CVD conditions. However, as the project progressed, a number of disturbing artifacts were observed that forced us to question the fundamental principles of emissivity-correcting

pyrometry. As a result, we embarked on a number of detailed investigations to verify that the physical principles behind the technique were applicable to our situation, and to also investigate all imaginable theoretical and experimental artifacts that could distort the measurement. This report summarizes the results of these studies. The end product of the project has yielded an instrument that no longer exhibits obvious artifacts and has already proved useful in improving MOCVD growth.

The report is divided into the following major sections: Fundamentals outlines the basic theory underlying pyrometry and derives the emissivity-correcting pyrometry formula used to extract a surface temperature from a measurement of the thermal emission and the reflectance. Basic elements of heat transfer that link total emissivity with surface temperature are also discussed. The Reflectance-correcting Pyrometer describes the design considerations in constructing a pyrometer and provides a schematic of the prototype instrument that was built. Investigations of Pyrometer Errors presents a detailed description of the measurement errors that can be encountered in pyrometry. Correcting Pyrometer Errors presents a method for measuring systematic errors *in situ* using a single fitting parameter. This parameter is effective at eliminating most of the experimental artifacts encountered when one uses a pyrometer in an enclosure. A short section, Measurements on Multiple Wafers discusses a specialty topic. The final section, Summary, collects all the important results together in a single place.

Some topics discussed within the main body of the text require considerable detail to fully develop the concepts. These details have been placed in appendices so that they do not distract the reader from the main points of the report.

1 Fundamentals

This section reviews the fundamental principles behind emissivity-correcting pyrometry and its application to the measurement of surface temperature during thin film growth. It also allows us to introduce the mathematical notation used to model the experimental data and derive algorithms for extracting temperature.

The authoritative reference on pyrometry is the excellent text by DeWitt and Nutter [1]. It carefully outlines the fundamental principles upon which radiation thermometry is founded. We will draw heavily from this text to derive the specific expressions that are needed to extract the surface temperature from a growing film. Another excellent text dealing with the fundamentals from an engineering aspect is Siegel and Howell [2]. Thermodynamic arguments used to derive Kirchhoff's law are dealt with in Drude [3] and Wood [4].

We start by first describing the properties of the purely idealized case of blackbody radiation and derive a formula for determining the temperature of a blackbody by measuring its thermal radiation. We then proceed to describe the thermal properties of real surfaces as manifested through the materials properties of absorptivity and emissivity. The link between real surfaces and the idealized blackbody radiation relations is then made through the application of Kirchhoff's law. This yields a simple formula for extracting temperature from the simultaneous measurement of the thermal radiation and specular reflectance. Finally, a brief discussion of the heat transfer phenomena that lead to the actual wafer surface temperature is made.

1.1 Blackbody Radiation

Planck [5] showed that a radiation field in thermodynamic equilibrium at an absolute temperature T has a radiation energy density (J/m^3) given by the following formula:

$$\rho(\lambda,T)d\lambda = \frac{8\pi ch}{\lambda^5}\frac{d\lambda}{e^{ch/\lambda kT}-1},$$

[1.1]

where λ is the wavelength, c is the speed of light, and h is Planck's constant. This formula can also be derived from quantum theory describing a Bose-Einstein statistical distribution of photons confined within a volume with a boundary of unspecified material; i.e. the nature of the thermalized radiation is independent of the material used to enclose it. By making a small opening in the cavity holding the thermally equilibrated radiation, it is possible to sample the radiation field. Such radiation is said to come from a "blackbody" because a small hole in a large cavity absorbs all radiation that falls on it, Fig. 1.1a. From thermodynamic arguments, it can be shown that no substance can emit thermal radiation with a higher radiance than a blackbody at the same temperature. It can also be proved that the radiation inside a blackbody cavity is unpolarized and isotropic. Emission of radiation from a perfect blackbody is thus completely diffuse, i.e. the flux per projected source surface area is independent of angle from the normal to the source, Fig. 1.1b.

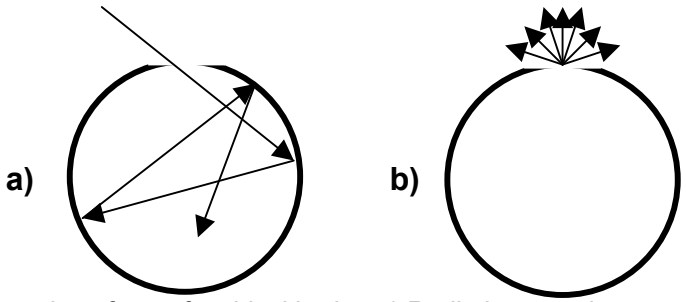

Fig. 1.1: Properties of a perfect blackbody. a) Radiation entering a small hole in a large cavity with absorbing walls has a negligible chance of exiting the hole. Hence, incoming radiation at all wavelengths and from any direction or polarization is totally absorbed within the cavity, making the hole appear completely black. b) Radiation at thermal equilibrium inside the cavity is isotropic. Hence, radiation exiting the cavity is completely unpolarized and diffuse. The spectral distribution of radiation depends only on the temperature.

The photometric spectral radiance, L_b (Watts•cm^{-2}•sr^{-1}•nm^{-1}) of blackbody radiation from the cavity hole is given by

$$L_b(\lambda,T)d\lambda = \frac{c_{1L}}{\lambda^5\left(e^{c_2/\lambda T}-1\right)}d\lambda\,,$$

[1.2]

where the "first radiation constant" is $c_{1L} = 1.191044\times10^{16}$ Watts•cm^{-2}•sr^{-1}•nm^4, and the "second radiation constant" is $c_2 = 1.438769\times10^7$ nm•K. Radiance is the fundamental quantity used to predict how much light flux can reach a detector. Radiance is conserved as it is imaged through an ideal optical system that has no transmission losses.

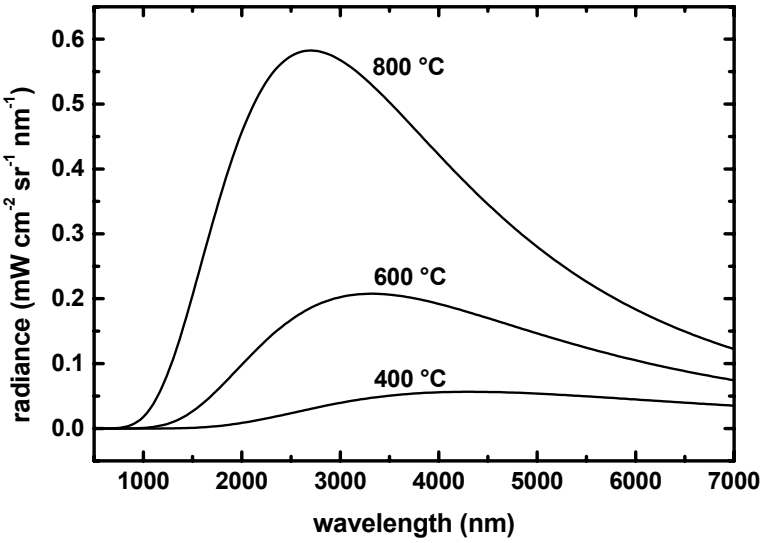

Fig 1.2: Spectral radiance distribution function of blackbody radiation.

Fig. 1.2. Shows a plot of the blackbody spectral radiance distribution given in Eq. [1.2] for several temperatures. Note that the curves never cross and that the wavelength of the maximum in the curve moves to shorter wavelength values as the temperature is increased. The wavelength of the maximum obeys "Wien's displacement law", $\lambda_{\max} = c_3 / T$, with the "third radiation constant", $c_3 = 2.8977\times10^6$ nm•K. The short-wavelength inflection point obeys a similar displacement law, with $\lambda_{\inf} = 1.70\times10^6 / T$.

1.2 Blackbody Pyrometry and the Wien Formula

A blackbody pyrometer extracts a temperature from a measurement of L_b by inverting Eq. [1.2]. Simple analytical formulas can be obtained by observing that the exponential term is much larger than 1 if $\lambda T << c_2$. Ignoring the "1" in Eq. [1.2] yields the Wien approximation formula for the spectral radiance

$$L_b(\lambda,T)d\lambda \cong \frac{c_{1L}}{\lambda^5} e^{-c_2/\lambda T} d\lambda \,,$$

[1.3]

which requires only a simple logarithm operation to determine the temperature from a measurement of $L_b(\lambda,T)$ over a narrow range of wavelengths. At the highest temperatures used for typical thin film deposition, 1200 °C, a pyrometer measuring radiance at 900 nm would incur an error of only 0.003 °C by using the approximation in Eq. [1.3]. The formula becomes more accurate at lower temperatures. Eq. [1.3] is the foundation for single-wavelength pyrometry.

The plots in Fig 1.2 might suggest that the best wavelength to monitor thermal emission is in the infrared, ~3000 nm, because the signals would be the largest there. However, it is more important to have high sensitivity when using a temperature probe. One wants the biggest possible percent change in a signal for a given percent change in temperature. Using the above Wien approximation, Eq. [1.3], the fractional change in thermal emission for a given fractional change in temperature is obtained by taking the derivative:

$$\frac{\partial L_b}{L_b} = \frac{c_2}{\lambda T}\frac{\partial T}{T} \,.$$

[1.4]

Eq. [1.4] states that the highest pyrometer sensitivity is obtained at short wavelengths and low temperatures. However, at some point a tradeoff will occur in which noise from a very small L_b signal will overwhelm the increased sensitivity gained by going to shorter wavelengths and lower temperatures. The optimum choice of detection wavelength is thus a balance between the shortest wavelength that still yields strong signals while maintaining a noise level well below the desired temperature sensitivity. As an example, a measurement of a 1 degree change from a 1000K blackbody will result in $\partial L_b / L_b = 14.4 / \lambda(\text{nm})$. This provides an easily measured 1.4%/K change at 1000 nm. The sensitivity would double to a 2.9%/K change at 500 nm, but the signal at 500 nm is 1.8×10^6 times smaller than the signal at 1000 nm! Because all detector/amplifier

combinations have some fixed noise "floor", the small signals encountered at short wavelengths will generate noise-to-signal ratios that exceed the sensitivity, making the measurement impossible.

1.3 The Single-wavelength Pyrometer

Fig. 1.3 shows a generic single-wavelength pyrometer schematic that employs a silicon detector. Silicon photodiodes provide an inexpensive, linear, and robust instrument. The spectral response of silicon extends to 1000 nm, peaking near 900 nm. Thus, 900 nm is a convenient wavelength that is on the short side of the blackbody curve, yet allows one to measure temperatures down to ~400 °C.

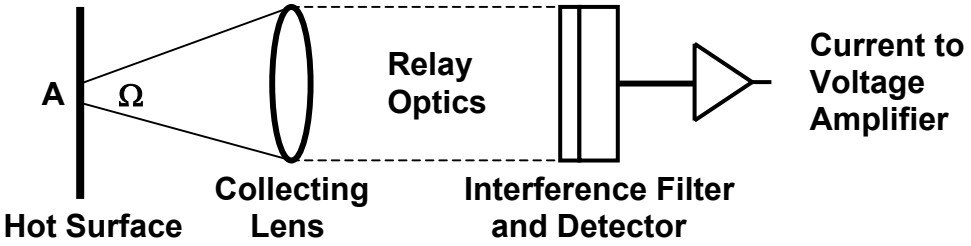

Fig 1.3: Schematic of a generic single-wavelength pyrometer. The product of viewing spot size, *A*, and solid angle of collection, Ω, determines the magnitude of the pyrometer signal. Relay optics may be lenses, mirrors, fiber optics, etc. A single wavelength is chosen with a narrow bandpass interference filter.

In addition to the detector sensitivity, the magnitude of the measured pyrometer signal is also governed by the amount of blackbody radiation that the instrument can gather. This is determined completely by two geometrical factors: The effective spot size that the pyrometer views on the blackbody surface, A (cm^2), and the solid angle covered by the collection lens, Ω (sr). Given a spectral bandpass for the detector, $\Delta\lambda$, and a detector sensitivity, S (Amps/Watt), the signal in Amps output by the detector is given by

$$signal = L_b \, \Delta\lambda \, A \, \Omega \, S \, . \qquad \textbf{[1.5]}$$

As an example, a 1000 K blackbody has (from Eq. [1.2]) a spectral radiance of 2.3×10^{-6} Watts•cm^{-2}•sr^{-1}•nm^{-1} at 900 nm. Using a 10 nm bandpass filter, a 0.5 cm viewing spot, a 1.5 cm dia collecting lens at 20 cm, and a detector sensitivity of 0.5 A/W, we obtain a signal current of 2.3×10^{-6} •10•π$(0.5/2)^2$•π$(1.5/2)^2/20^2$•0.5 = 9.97 nA. This signal is readily measurable with a high (10^4) signal-to-noise ratio.

Fig. 1.4 plots the expected signal from the pyrometer described above over a temperature range typically used in MOCVD applications. Note that the relatively healthy signal of 10 nA obtained at 700 °C shrinks to 4 pA at 400 °C. The high sensitivity of pyrometry thus comes at a cost of high dynamic range for the signal electronics. The curvature in the semi-log plot demonstrates the falloff in sensitivity at higher temperatures expressed in Eq. [1.4]. Note also that the signal displayed in Fig 1.4 represents the largest value that could ever be received for the given geometry because real materials always emit less radiation than an ideal blackbody.

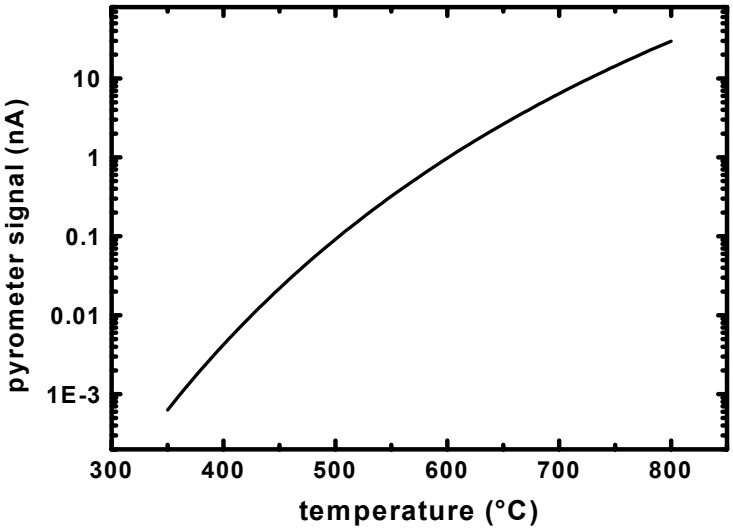

Fig 1.4: Expected signal from a 900 nm blackbody pyrometer over a temperature range typically used in MOCVD applications.

In practice, there are losses and unknown factors within the pyrometer such that the purely geometrical arguments used above are inadequate to accurately calibrate temperature measurement with the pyrometer shown in Fig 1.3. However, from Eq. [1.3] we have the following rigorous relationship between a thermal emission signal, s, measured at a single wavelength, λ, and the temperature, T.

$$s = Ce^{-c_2/\lambda T}.$$

[1.6]

The constant C includes all wavelength, geometry, attenuation, and sensitivity factors. C may be empirically determined by calibrating the pyrometer with a commercial blackbody furnace. The furnace is basically a cavity equipped with a thermocouple that allows one to measure a thermal radiation signal, s_{cal}, at a known temperature, T_{cal}. By inverting Eq. [1.6], one can obtain the following formula for determining temperature from a measured signal, s, given the measured calibration signal, s_{cal}, and the known temperature, T_{cal}:

$$\frac{1}{T} = \frac{1}{T_{cal}} - \frac{\lambda}{c_2}\ln\frac{s}{s_{cal}}.$$

[1.7]

Eq. [1.7] is the working equation used in commercial blackbody pyrometers, calibration having been done by the manufacturer.

1.4 Radiation from Surfaces of Real Materials

Pyrometry of a blackbody is not very useful because a blackbody is an idealization which can only be approached with the cavity structure shown in Fig. 1.1. The behavior of real materials and real surfaces adds significant complexity to pyrometry. Below is a discussion of methods that have been developed to handle real materials and how pyrometry can be done with them. Some of the concepts are deceptively simple, but turn out to be subtle details crucial in determining whether pyrometric methods are valid for thin film deposition conditions.

1.4.1 Absorptivity

Fig 1.1a illustrates that a blackbody is a perfect absorber of radiation at all wavelengths, incidence angles, and polarizations. It is well known that all real surfaces absorb different amounts of energy depending on the wavelength, λ, and incidence angle, θ. Some anisotropic or machined surfaces may even have absorption that depends on the azimuthal angle, φ. Smooth dielectric surfaces such as those used in semiconductor manufacturing exhibit strong differences in absorption for light polarized perpendicular ("*s*") or parallel ("*p*") to the plane of incidence. Any real surface thus departs from the ideal blackbody in many aspects.

The absorption properties of a real material may be quantified by defining the spectral absorptivity of a surface, $\alpha(\lambda,\theta,\varphi,\sigma,T)$, as the fraction of electromagnetic energy absorbed by a material at temperature, T, when exposed to a beam of radiation with wavelength λ, incidence angle θ, azimuthal angle φ, and polarization σ. For a blackbody, $\alpha = 1$, independent of λ, θ, φ, σ, or T. For a real material, $\alpha \leq 1$, and α can be a strong function of all the parameters above. Absorptivity is considered to be an intrinsic property of both the material and the condition of its surface. Surface condition can often dominate over the intrinsic absorption properties of the bulk material. For example, copper, which is nearly a perfect reflector in the infrared can have its surface oxidized with a special process that yields an absorptivity of nearly one for applications in solar panels. Multiple-layers of transparent thin films may be placed on an absorbing substrate to create a non-absorbing surface with near unity reflectivity over a limited range of wavelengths.

In the absence of non-linear material-radiation interactions, such as would occur from illumination with high power lasers, the intensity or spectral distribution of the light used to measure absorptivity is not important. The value of the absorptivity is thus the same for a given substance independent of whether the incident radiation used to measure it is from a lamp, fluorescent light, weak laser beam, or blackbody cavity irradiation. This seemingly trivial observation turns out to be a key argument in using Kirchhoff's law to derive useful pyrometry formulas.

1.4.2 Emissivity

For the same reasons that no real surface can absorb like a blackbody, no real surface will emit pure blackbody radiation when heated. As with absorption, we describe thermal emission from a real surface with another material/surface property, the emissivity, $\varepsilon(\lambda,\theta,\varphi,\sigma,T)$. Emissivity is defined to be the fraction of thermal radiation emitted by a surface at wavelength λ, exit angle θ, azimuthal angle φ, polarization σ, and temperature, T, compared to a blackbody at the same temperature, T, and wavelength, λ. In a thought experiment, the emissivity is measured by first

recording a signal from a blackbody cavity (Fig 1.1b), then measuring the signal from a real heated surface in a specified direction with a specified polarization. The ratio of these two signals is defined to be the emissivity. A blackbody has $\varepsilon = 1$ for all conditions. Thermodynamic arguments yield the conclusion that $\varepsilon \leq 1$ for all real materials.

Another way to express the definition for emissivity is with the following equation:

$$L(\lambda,\theta,\varphi,\sigma,T) = L_b(\lambda,T)\varepsilon(\lambda,\theta,\varphi,\sigma,T),$$

[1.8]

where $L(\lambda, \theta, \varphi, \sigma, T)$ is the spectral radiance of a real surface at wavelength λ, normal angle θ, azimuthal angle φ, polarization σ, and temperature T. It is thus possible for a real surface to emit radiation that departs significantly from the blackbody spectral distribution given in Eq. [1.2] and to also emit different amounts of energy in various directions. The thermal emission from real surfaces can also be polarized.

1.5 *Emissivity-correcting Pyrometry*

Eq [1.8] is not much different than the blackbody expression for radiance. If the emissivity can somehow be independently measured, then Eq. [1.8] and Eq. [1.3] may be combined to obtain an equation for the temperature. This process is referred to as emissivity-correcting pyrometry. This section presents a detailed derivation of the emissivity-correcting pyrometry equation for the special case of surface temperature measurement during the growth of thin films on smooth, flat, opaque substrates. First, an exact result is obtained that relates the spectral, directional emissivity to the spectral, directional absorptivity. Second, three reasonable assumptions are made about the nature of the semiconductor wafer surface in order to obtain an expression for the spectral directional emissivity in terms of an easily-measured specular reflectance. This finally leads to a simple equation for emissivity-correcting pyrometry.

1.5.1 Kirchhoff's law

The connection between blackbody pyrometry and the pyrometry of real surfaces is made using Kirchhoff's law, which is simply the application of energy conservation and thermodynamics to derive a relationship between emissivity and absorptivity.

Consider the thought experiment illustrated in Fig. 1.5. A substance is placed inside a blackbody cavity and is allowed to come to thermal equilibrium. At equilibrium, the temperature of the substance is the same as the cavity and the thermal radiation in the cavity. The radiation inside the cavity is isotropic, unpolarized blackbody radiation with a spectral distribution given by Eq. [1.1] and a function only of the cavity temperature. Now consider the energy balance that must be present in order for the substance to maintain a constant temperature. In a given direction, the differential loss per second in energy by radiation at wavelength λ, exit angle θ, azimuthal angle φ, polarization σ, and temperature, T is given (from Eq. [1.8]) by

$$loss = L_b(\lambda,T)\varepsilon(\lambda,\theta,\varphi,\sigma,T)d\lambda\, dA\, d\Omega\,.$$

[1.9]

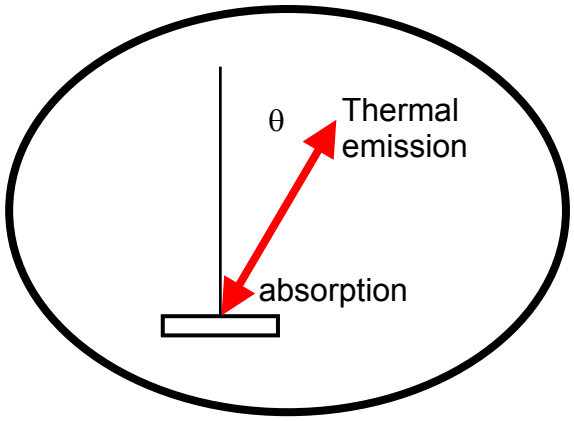

Fig 1.5: A substance is placed inside a blackbody cavity and is allowed to come to thermal equilibrium. The energy lost due to radiation from the surface in a specific direction must be exactly balanced by the energy gained from blackbody irradiation in the same direction, but opposite flow, in order for the radiation field to remain isotropic and the temperature of the substance to remain constant. This relationship is individually true for every direction, wavelength, and polarization.

The differential gain in energy per second due to irradiation of the surface by the blackbody radiation in the cavity at the same angles and polarization, but opposite energy flow is given by

$$gain = L_b(\lambda,T)\alpha(\lambda,\theta,\varphi,\sigma,T)d\lambda\, dA\, d\Omega\,.$$

[1.10]

Both Eq. [1.9] and Eq [1.10] simply use the definitions of ε and α to compute the power either emitted or absorbed. Because blackbody radiation is isotropic, the same value, $L_b(\lambda,T)$, is used for all angles and polarizations in both equations. If the substance is to remain at a constant temperature, and the blackbody radiation field is to remain isotropic in the cavity, the differential energy loss due to radiation must be exactly balanced by energy gain due to absorption. Kirchhoff's law then states that, for <u>all</u> real materials,

$$\alpha(\lambda,\theta,\varphi,\sigma,T) = \varepsilon(\lambda,\theta,\varphi,\sigma,T).$$

[1.11]

Note that the equality exists <u>individually</u> for <u>every</u> wavelength, direction, and polarization, <u>provided that identical parameters are used as the arguments for α and ε</u>. It says nothing about the relationship, for example, between $\alpha(\theta_1)$ and $\varepsilon(\theta_2)$. This constraint has important implications in pyrometry applications, as will be seen below

Eq. [1.11] yields a profound and subtle result. The equality must be true to be consistent with energy conservation and thermodynamics as derived in the above thought experiment inside a blackbody cavity at equilibrium. However, we recognize that both ε and α are just materials properties. Their definitions remain the same independent of whether the material is inside a blackbody cavity or not (see the definitions for Absorptivity and Emissivity above). The equality must therefore hold even if the substance is not in thermal equilibrium with blackbody radiation. Eq. [1.11] allows one to determine the value of the emissivity (which is quite difficult to measure in practice) by measuring the absorptivity instead. Of course, one must be careful to

measure α with the same set of parameter arguments, but measurement in a blackbody cavity is not required.

Exceptions to Eq. [1.11] can be produced under extreme non-equilibrium conditions. For example, irradiation of a substance with a femtosecond laser can cause α to not be equal to ε because the surface of the material does not have enough time to establish a local thermalized state with a meaningful definition of temperature. This violates the equal-argument condition implicit in Kirchhoff's law (the temperatures are not the same). However, for thin film deposition conditions, the chemistry that takes place on the surface of the wafer may be described in terms of a meaningful local surface temperature, T, despite the fact that the entire deposition chamber is not strictly in global equilibrium. In other words, if the temperature of the surface is a meaningful concept, then Eq. [1.11] is unconditionally true. If the surface temperature is not defined, then the concept of pyrometry is also invalid. In thin film deposition applications we will never encounter a situation in which Eq. [1.11] cannot be used for pyrometry.

In applications outside the scope of this report, various relations between ε and α are used in which averaging is done over one or more variables, eg. "hemispherical emissivity", which averages over θ and φ. These less general relationships have further conditions attached to them that might invalidate their use for some materials systems. We are careful to avoid these special cases and concentrate instead on using the unconditional differential, spectral expressions given by Eq. [1.11] to derive formulas for emissivity-correcting pyrometry.

1.5.2 Absorptivity and specular reflectance

Kirchhoff's law allows us to measure emissivity by measuring absorptivity. Measuring absorptivity does not require a specialized blackbody radiation reference source, but it still can be difficult to determine because α may have complex angle, wavelength, and polarization dependencies. It is also difficult to directly measure absorption of energy. However, by using three assumptions that are very reasonable for applications to pyrometry of thin film growth, the measurement of absorptivity can be made with a simple measurement of specular reflectance.

Energy conservation constrains a propagating beam of light striking the surface of any material to obey the following general expression:

$$\rho(\lambda,\theta,\varphi,\sigma;2\pi)+\alpha(\lambda,\theta,\varphi,\sigma)+\tau(\lambda,\theta,\varphi,\sigma;2\pi)=1\,. \qquad \textbf{[1.12]}$$

ρ is the "hemispherical reflectance". This is the fraction of light scattered into all possible angles above the surface, given an incident beam with incidence angle θ, azimuthal angle φ, and polarization, σ. Reflectance is a bi-directional property. It can range from perfectly diffuse reflectance that scatters an incident beam into all 2π steradian directions to a perfectly specular behavior that reflects only at the same angle as the angle of incidence. α is the absorptivity of the material. τ is the "hemispherical transmittance". This is the fraction of light transmitted through the substance into all possible angles below the surface.

We now simplify Eq. [1.12] with three assumptions specifically applicable to thin film semiconductor growth.

- Our first assumption is that the semiconductor wafer is opaque, $\tau = 0$. If a pyrometry wavelength is chosen too far below the bandgap of a substrate, this assumption may not be valid. However, it is generally possible to choose an above-bandgap wavelength for all but a few (eg GaN) semiconductors.
- Our second assumption is that the wafer remains smooth and flat during deposition. Under these conditions, an incident beam of light will scatter only in the specular direction and the reflected light beam is easily measured. If the surface becomes rough during deposition, then the formulas that follow are not valid. We require a smooth enough surface that one may measure the hemispherical reflectance, ρ, with a simple specular beam reflectance probe. It is impossible to directly measure the hemispherical reflectance of a rough surface during deposition (for example, with an integrating sphere) because of the limited optical access in a CVD chamber.
- Our third assumption is that the specular reflectance does not depend on azimuthal angle, φ. This is generally true for compound semiconductors for which the reflectance anisotropy is typically less than one part in a thousand. This assumption is not strictly necessary to relate absorptivity to specular reflectance, but is convenient for practical applications on rotating wafers.

With the three above assumptions, Eq [1.11] and Eq. [1.12] simplify to

$$\varepsilon(\lambda,\theta,\varphi,\sigma,T)=\alpha(\lambda,\theta,\varphi,\sigma,T)=1-R(\lambda,\theta,\sigma,T),$$

[1.13]

where $R(\lambda, \theta, \sigma, T)$ is the specular reflectance of the wafer. Eq. [1.13] gives us an easily-executed method to determine $\varepsilon(\lambda, \theta, \varphi, \sigma, T)$ for thin film deposition applications. Note that for Eq. [1.13] to be accurate, measurements of R must be made under the same conditions (i.e. wavelength, angle, and polarization) as the measurements of thermal emission. Otherwise, the conditions of Kirchhoff's law are violated.

1.5.3 The reflectance-correcting pyrometer equation

Combining Eqs.[1.3], [1.8], [1.11], and [1.13] yields

$$L(\lambda,\theta,\sigma,T)d\lambda=\left[1-R(\lambda,\theta,\sigma,T)\right]\frac{c_{1L}}{\lambda^5}e^{-c_2/\lambda T}d\lambda\ .$$

[1.14]

Eq. [1.14] is the emissivity-correcting pyrometry expression for a smooth, flat, opaque surface. It relates a thermal emission spectral radiance, L, and a specular reflectance, R, to the surface temperature, T. An equation analogous to Eqs. [1.6]and [1.7] may be derived, based on a calibration of the pyrometer at a known temperature, T_{cal}, and known substrate reflectance, R_{cal}:

$$\frac{1}{T} = \frac{1}{T_{cal}} - \frac{\lambda}{c_2} \ln \frac{s\left(1 - R_{cal}\right)}{s_{cal}\left(1 - R\right)}.$$

[1.15]

To emphasize that assumptions are built into Eqs. [1.14] and [1.15], we refer to the above pyrometer expressions as "reflectance-correcting pyrometry", and the instrument used to measure temperature with this method as a "reflectance-correcting pyrometer".

Eq. [1.14] is a rigorous, fundamental expression that relates the physical quantities L and R to the surface temperature, T. Eq. [1.15] is an algebraic inversion of Eq. [1.14] that implicitly assumes that the measured s is proportional to L and that the absolute reflectance is measured exactly. We see that the $(1 - R)$ factor in Eq. [1.15] is used to effectively cancel the emissivity factor that is present in the thermal emission, Eq. [1.8]. For this to be effective, one must ensure that the constraints of Kirchhoff's law are adhered to as closely as possible: The wavelength, angle, and polarization used to measure the s and R signals must be the same. The rest of this report essentially deals with the experimental subtleties encountered in going from Eq. [1.14] to Eq. [1.15].

1.6 Heat Transfer and Surface Temperature

The surface temperature that is measured by the reflectance-correcting pyrometer is determined by a steady-state balance between energy flows to the wafer and energy losses from the wafer. In this section we briefly discuss the heat transfer properties of a rotating disk reactor (RDR), which is the MOCVD reactor design used in this report. In addition to the usual conductive/convective losses typically associated with heat transfer problems, one also has significant energy losses due to thermal radiation. Because the thermal radiation is tied to emissivity, Eq. [1.8], there is an intimate connection between the steady-state surface temperature and the state of the thin-film structure on the wafer surface. Because radiation is instantaneous, emissivity changes on the wafer translate instantaneously to changes in radiative losses. This can lead to small steady-state surface temperature changes that may be difficult to control with a remote, sluggish heater.

1.6.1 Energy gains

The energy flux to the wafer is difficult to model because it consists of multiple thermal resistances in series. Starting at the heater filament, energy must pass through a gas-filled gap to the wafer carrier, through the wafer carrier, through a small gap between the carrier and the wafer, and finally to the wafer surface. The gas-filled gaps have heat transfer coefficients that are difficult to model because the gas is of unknown composition, flow patterns between the filament and carrier are unknown, and the exact carrier-to-wafer gap is unknown and possibly variable. Fortunately, we do not need to perform such modeling in order to determine small surface temperature changes. One need only assume that there exists an energy flux, q_{in}, to the wafer surface.

1.6.2 Energy losses

Energy losses are more straightforward to model. The heat flux from the wafer surface is the sum of conductive/convective losses due to rotating disk action and radiative losses due to thermal emission. Both of these phenomena depend on the wafer surface temperature. The

radiative losses depend on the value of the "total hemispherical emissivity". This is the emissivity of the surface integrated over all exitance angles, all wavelengths, and both polarizations. Perturbations of the total hemispherical emissivity, such as thin film growth, can thus alter the heat transfer characteristics and the surface temperature of the wafer. If the disk is heated to a very high temperature, radiative losses dominate the heat transfer and are given approximately by the Stephan-Boltzmann equation:

$$q_{rad} = \varepsilon_{tot}\sigma_{sb}T^4$$

[1.16]

where σ_{sb} is the Stephan-Boltzmann constant.

1.6.3 Surface temperature changes during film deposition

The following qualitative argument is posed to describe the relationship between surface temperature and changes in the total hemispherical emissivity, ε_{tot}. Under steady-state conditions the energy gains are equal to the energy losses, $q_{in} = q_{rad}$. If ε_{tot} changes during film deposition, Eq. [1.16] states that the heat loss would have to change if the surface temperature remains constant. However, over short periods of time, the heater will continue to provide an energy flux of q_{in}, which effectively does not let q_{rad} change. Energy balance therefore requires that the surface temperature adjust itself to satisfy $q_{in} = q_{rad}$ and Eq. [1.16]. A decrease in ε_{tot} will cause an increase in T and visa-versa.

Appendix A provides a more quantitative derivation of surface temperature changes. It includes conductive/convective losses as well a more accurate expression for radiative heat loss. The result is a quartic equation for the wafer temperature when the surface is perturbed with total hemispherical emissivity changes. It is possible for perturbations in the local environment at the wafer surface to cause temperature changes that are never "seen" by the heater controller. The highest accuracy wafer temperature monitoring and control is therefore best done by actually measuring at the wafer surface.

1.7 Two color Pyrometry

Textbooks often site an attractive method, called "two-color pyrometery" for dealing with the emissivity problem. The idea is to measure thermal emission at two different wavelengths, $s_1(\lambda_1)$ and $s_2(\lambda_2)$. Provided that the chosen wavelengths are not too different from each other, it is possible that the emissivity is very close to the same value at each wavelength. This condition is called the "greybody" approximation:

$$\varepsilon(\lambda_1) = \varepsilon(\lambda_2).$$

[1.17]

If Eq. [1.17] is true, then the emissivity may be easily eliminated by taking the ratio of the two thermal emission signals. This yields a simple expression that contains only the ratio, wavelengths, and the temperature:

$$\frac{s_2}{s_1} = C\frac{L_2}{L_1} = \hat{C}e^{\frac{c_2}{T}\left(\frac{1}{\lambda_1}-\frac{1}{\lambda_2}\right)}.$$

[1.18]

Unfortunately, very few true greybodies can be found in real-world pyrometer applications, so Eq. [1.18] is more of an interesting academic exercise than a practical emissivity correcting scheme. Eq. [1.17] is virtually guaranteed to *never* be true in thin film deposition applications because the emissivity exhibits strong wavelength-dependent interference effects during growth. Sensitivity analysis of the two color method (see ref [1]) reveals that very large errors, sometimes exceeding 100 °C, will be encountered if one chooses to use the two-color pyrometer method on thin film applications. We therefore reject this method in favor of the reflectance-correcting scheme in which no greybody assumptions need to be made.

2 The Reflectance-correcting Pyrometer

This section describes the application of the fundamental reflectance-correcting pyrometry relations, Eqs. [1.14] and [1.15], to the design of an instrument that can accurately measure temperature during thin film growth. Whereas Eq. [1.14] may be considered to be essentially exact, it is difficult to actually measure L and R without some compromises that affect accuracy. The use of Eq. [1.15] is therefore subject to constraints imposed by these compromises. This section, and the rest of the report, quantifies the constraints with increasing levels of detail.

2.1 Optimum Measurement of Emission and Reflectance

Any real measurement of thermal emission or reflectance cannot measure L or R at a single wavelength, angle, and polarization, as Eq. [1.14] implies. Instead, one must collect light over a range of wavelengths, angles, and polarization states. The measurement of a physical quantity also necessarily requires a detector that transforms optical radiation into a proportional electrical signal. The measured thermal emission signal, s, is given by:

$$s = \int_{\Delta\lambda,\Delta\theta,\Delta\sigma} f(\lambda,\theta,\sigma)L(\lambda,\theta,\sigma,T)d\lambda d\theta d\sigma ,$$

[2.1]

and the measured specular reflectance signal, r, is given by

$$r = \int_{\Delta\lambda,\Delta\theta,\Delta\sigma} g(\lambda,\theta,\sigma)R(\lambda,\theta,\sigma,T)d\lambda d\theta d\sigma ,$$

[2.2]

where $\Delta\lambda$, $\Delta\theta$, and $\Delta\sigma$ represent the range of wavelengths, angles, and polarization states spanned by the measurement process. f and g are instrument response functions. If the ranges are significantly large, a simple algebraic inversion of Eq. [1.14] to yield Eq. [1.15] is not possible. In fact, Eq. [1.15] is strictly valid only in the limit of $\Delta\lambda = \Delta\theta = 0$, and with perfect polarization, which, of course is impossible in practice. Under the best conditions, f and g are very nearly δ-functions, allowing Eq. [1.15] to be an essentially exact inversion of Eq. [1.14].

In order to use the convenient expression in Eq. [1.15], one must use ranges that are as small as possible and choose an experimental arrangement in which L and R change as little as possible over the measurement range. One must also conform to the constraints of Kirchhoff's law: measurements of s and R must be made with the same set of λ, θ, and σ values so that the emissivity term inherent in s is divided away by the $(1 - R)$ factor in Eq. [1.15]. The following general considerations are made to address the optimum measurement of s and r with the least sensitive $\Delta\lambda$, $\Delta\theta$, and $\Delta\sigma$ ranges.

2.1.1 Incidence angle and polarization

As shown in Fig. 2.1, light polarization effects can be particularly troublesome with semiconductor materials. Very large differences in reflectance are manifested between s and p

polarized light, and small changes in incidence angle can lead to substantially different reflectance values. In fact, dielectric surfaces were some of the earliest-used polarizing devices. The sensitivities pictured in Fig 2.1 complicate the modeling and affect the accuracy of a pyrometer. However, at normal incidence, $\theta = 0$, the *s* and *p* curves merge. Virtually no change in the reflectance is observed for unpolarized light for incidence angles less than 6 degrees. As a result, polarization considerations may be eliminated altogether by choosing normal incidence for a pyrometer.

The weak dependence of reflectance on incidence angle at normal incidence also allows one to collect thermal emission over several degrees, yet maintain the close approximation: $\langle L \rangle_\theta \cong L(\theta = 0)$. For example, the unpolarized reflectance of GaAs is 0.318936 at zero degrees and is the same value to six digits at 2.15 degrees (15 mm diameter window at 200 mm). (Individual *s* and *p* components are 0.319186 and 0.318686, respectively). Because the thermal emission signal is directly proportional to the solid angle of light collection, the largest possible signal may be gathered with the least angle-sensitivity error using normal incidence. In fact, collection of the signal at normal incidence is so insensitive to angle and polarization, we may safely assume that the instrument functions take on the much simpler forms:

$$f(\lambda, \theta = 0, \sigma) \cong f(\lambda)\delta(\theta); \qquad g(\lambda, \theta = 0, \sigma) \cong g(\lambda)\delta(\theta) \qquad \textbf{[2.3]}$$

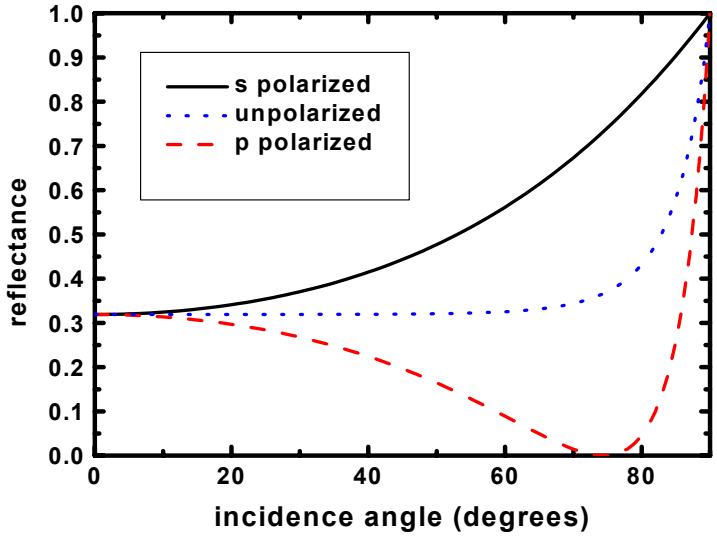

Fig 2.1: 900 nm reflectance from a GaAs semiconductor surface as a function of incidence angle. Light with the electric field vector polarized perpendicular to the plane of incidence is called "s-polarized", and light with the electric field vector polarized parallel to the plane of incidence is called "p-polarized". The reflectance is least-sensitive to angle and polarization effects at normal incidence, $\theta = 0$.

2.1.2 Wavelength range

The size of the thermal emission signal is proportional to the bandwidth of radiation that the detector is allowed to measure. There is thus a tradeoff between signal strength and the need to keep $\Delta\lambda$ as small as possible. Bandwidth effects can be significant in single-wavelength pyrometry. Fig. 2.2 compares the spectral dependence of a gaussian bandpass filter with FWHM 50 nm to the product of this filter with a 550 °C blackbody radiance curve (right scale). From Eq. [2.1], the signal, *s*, is obtained by measuring over the interference-filter-blackbody-radiance product. As seen in Fig. 2.2, the shape of the blackbody radiance curve causes more signal to pass through the longer-wavelength part of the interference filter. If Eq. [1.15] is used to extract a temperature, a value of 798.03° is obtained for a 800 °C blackbody surface calibrated at 550 °C.

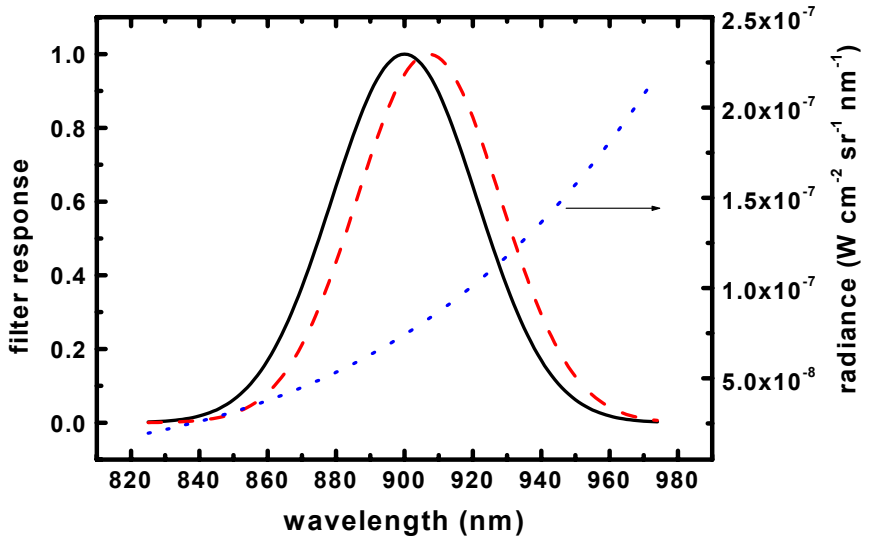

Fig 2.2: Solid curve: Spectral distribution function of a 50 nm gaussian bandpass filter. Dashed curve: Normalized product of the filter times the blackbody radiance distribution function at 550 °C (dotted curve, right scale). The integrated signal received through such a filter has an effective bandpass maximum at 905 nm rather than 900 nm. The effective maximum will vary with temperature.

The apparent shift in the filter lineshape shown in Fig. 2.2 leads to a commonly used correction scheme for wide-bandpass pyrometer instruments called the *effective wavelength approximation* [1]. Using 905.484 nm instead of 900 nm in Eq. [1.15], the correct temperature of 800.000 °C is obtained. Unfortunately, a different effective wavelength is needed for each temperature, determined by iteration. DeWitt and Nutter [1] outline how the effective wavelength may be computed for greybody pyrometer applications. As with two-color pyrometry, discussed above, the presence of thin films invalidates the use of effective wavelength methods. Spectral features caused by thin film interference affect the integrated signal in complex ways.

If the bandwidth of the filter is reduced to 10 nm, then Eq. [1.15] yields a value of 799.92 for a 800 °C blackbody surface calibrated at 550 °C. The errors with a 10 nm bandpass filter are thus small enough to allow one to ignore the complications of effective wavelength.

2.1.3 Error analysis of Eq. 1.15

Provided that the emission signal and reflectance can be measured over the smallest possible parameter ranges and the least sensitivity to parameter conditions, as indicated in Eq. [2.3], it remains to be seen how sensitive the temperature measurement is to the quantities s and R in Eq. [1.15]. We have the general mathematical relationship for any function of two variables:

$$\Delta T(s,R) = \frac{\partial T}{\partial s}\Delta s + \frac{\partial T}{\partial R}\Delta R\,.$$

[2.4]

Applying this to Eq. [1.15] yields:

$$\Delta T(s,R) = \frac{\lambda T^2}{c_2}\frac{\Delta s}{s} + \frac{\lambda T^2}{c_2}\frac{\Delta R}{1-R}\,.$$

[2.5]

For typical conditions, $\lambda = 900$ nm, $T = 1000$ K, the above expression reduces to

$$\Delta T(s,T) \cong 60\frac{\Delta s}{s} + 60\frac{\Delta R}{1-R}\,.$$

[2.6]

A 1% error in the thermal emission signal will give only a 0.6° error in the temperature. The pyrometer is thus not very sensitive to errors in the thermal emission signal.

An absolute error of 0.01 reflectance units results in different temperature errors, depending on the value of the reflectance. The table below lists the estimated temperature errors from Eq. [2.6] for different values of R:

R	ΔT (°C)
0	0.6
0.1	0.66
0.4	1
0.8	3
0.9	6
0.99	60

Clearly, conditions with high reflectance values are expected to yield the most inaccurate temperatures and will be most sensitive to errors and noise in the reflectance. Another way to look at this problem is to calculate the deviation in reflectance that would be needed to produce a small change in temperature. For $R = 0.95$, a 0.5° error in temperature requires only a 4×10^{-4}

error in absolute reflectance. Extraordinary accuracy in the absolute reflectance would therefore be required to maintain a temperature accuracy of less than a degree at high reflectance values. On the other hand, substantial (1%) errors in the reflectance can be tolerated without affecting the temperature by more than a degree if $R < 0.3$. Temperature errors encountered with the virtual pyrometer experiments (see 3.3.1) bear out the predictions of this simple error analysis. Every effort should be made to minimize errors in the absolute reflectance signal.

In theory, it is impossible to determine the surface temperature with a single wavelength pyrometer when $R = 1$, because s is zero. Under these conditions, the wafer emits no light at the pyrometer wavelength, independent of the surface temperature. It is not surprising, therefore, that the biggest errors in temperature measurement will occur at high reflectance conditions. The small emission signal, high-reflectance conditions are also most susceptible to errors from stray light and instrumental artifacts. These effects are discussed in more detail in sec 3.

2.2 *Reflectance-correcting Pyrometer Instrument*

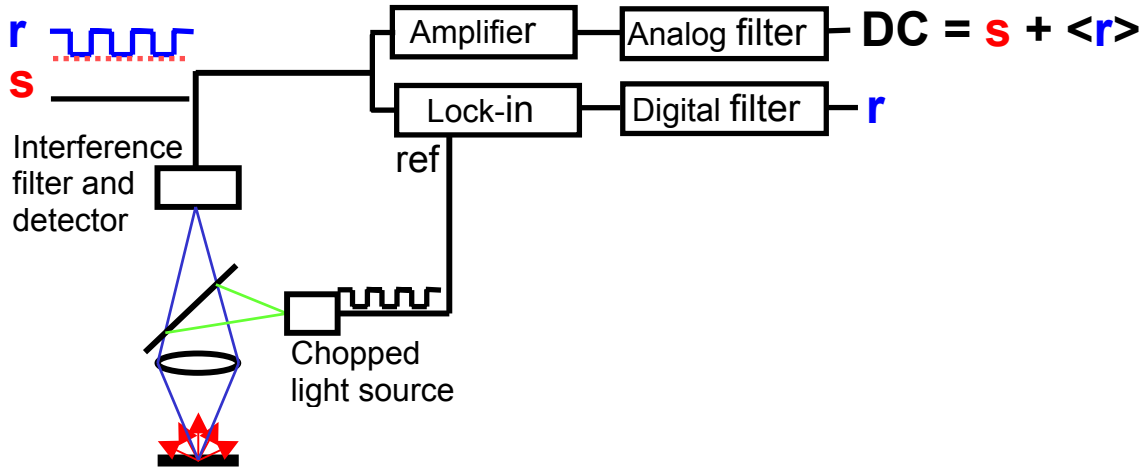

Fig 2.3: Schematic of the reflectance-correcting pyrometer. The thermal emission signal, **s**, is measured at normal incidence through a 10 nm bandpass interference filter and a silicon photodiode with an amplifier and low-pass analog filter. Reflectance is measured by chopping a light source beam, launching the beam co-linearly with the thermal emission optical axis using a beamsplitter and detecting the reflected signal, **r**, with a lock-in amplifier. The DC signal contains the sum of the thermal emission signal and the average of the reflectance signal, but the two may be separated with calibration and software.

An instrument has been built to satisfy most of the conditions imposed by the above sensitivity and error analysis. A schematic of this instrument is shown in Fig. 2.3. We have chosen normal incidence to minimize the effects of wafer tilt angle and eliminate polarization effects. The collection optics are limited by a 15 mm dia. window at roughly 200 mm from the surface, limiting the range of incidence angles to a maximum of 2°. This effectively reduces the instrumental functions to the wavelength-only expressions in Eq. [2.3]. The wavelength-dependent instrument functions are reduced to nearly δ functions by using a 10 nm bandpass interference filter at 900 nm. The light source, beamsplitter unit, and detector are connected with single-core, multi-mode optical fibers.

To ensure that we are taking the correct advantage of Kirchhoff's law as stated in Eq. [1.11], a beamsplitter arrangement was chosen. This arrangement has the practical advantage that only a single window is required, which is important for most deposition systems in which optical access is at a premium. The beamsplitter provides identical optical paths for the thermal emission and the reflected light from the surface of the wafer to the detector ($\alpha(\theta)$ and $\varepsilon(\theta)$ must have identical θ's). The identical optical path condition also ensures that the thermal emission and reflectance are measured from the same spot on the wafer. By using the same interference filter and detector for both the *s* and *r* signals, one ensures that the shapes of the instrumental functions $f(\lambda)$ and $g(\lambda)$ are absolutely identical ($\alpha(\lambda)$ and $\varepsilon(\lambda)$ must have identical λ's).

The configuration shown in Fig. 2.3 conforms closely to theoretical considerations necessary to perform accurate reflectance-corrected pyrometry. However, this choice of data collection complicates the signal gathering electronics because the same detector is used to measure both the thermal emission and reflectance signals. To separate the signals, the reflectance source is chopped and its value is extracted using a lock-in amplifier referenced to the chopping frequency. The DC component of the signal contains the thermal emission signal and the DC average of the reflectance signal. The reflectance component may be subtracted from the DC signal using calibration procedures described below. The advantage of a physically-optimized beam-splitter arrangement is thus countered by the complexity of "de-multiplexing" the mixed electronic signals that result. In practice, this instrumental complexity is not too high a price to pay for accurate temperatures.

2.2.1 Signal separation and calibration

We choose to calibrate the pyrometer shown in Fig. 2.3 with an *in situ* procedure. This differs from many commercial instruments that calibrate against a blackbody furnace at the manufacturer's facility. *Ex situ* calibrations do not account for losses in windows and one-of-a-kind quirks in the light-gathering process that exist with any instrument that is mounted on a reaction chamber.

One needs a bare substrate wafer with a known reflectance at room temperature to perform the calibration. The *in situ* calibration is not difficult and needs to be performed only periodically. Because stray light effects unique to the deposition chamber (and even different wafer carriers) must be accounted for, offline calibration is impossible anyway. We discuss below the basic calibration procedure, ignoring stray light effects. The additional steps needed to account for stray light, correcting for temperature overcompensation, are discussed in 4.3

There are actually two calibration procedures that must be performed with the reflectance-correcting pyrometer. The first, termed the "*s*" calibration, measures the sensitivity for the thermal emission signal, *s*, effectively determining *f* in Eq. [2.1]. This procedure uses the measured thermal emission signal at a known wafer temperature. It needs to be performed only intermittently as the reactor ages and stray light effects slowly change. The second, termed the "*r*" calibration, determines the sensitivity for the reflectance signal, *r*, effectively determining *g* in Eq. [2.2]. This calibration is easily performed for every run by scaling the reflectance signal at the beginning of the run with a factor that gives the known starting reflectance of the substrate wafer.

The pyrometer records two signals. The signal from the lock-in is simply r, which is proportional to the absolute reflectance, R. One need only determine a calibration factor, R_{fac}, to determine the reflectance for a given measured value of r:

$$R = R_{fac} r \,.$$

[2.7]

The second signal is a DC average of the thermal emission and reflected light signals. It may thus be expressed as the sum of the thermal emission signal, s, and an instrumental term that is proportional to r:

$$DC = s + ar$$

[2.8]

One must determine the factor, a, in order to obtain the desired signal, s, from

$$s = DC - ar$$

[2.9]

Once the two instrumental factors, R_{fac} and a, are determined, the pyrometer may be calibrated for temperature measurements in the MOCVD reactor.

Using a bare substrate whose room-temperature reflectance is known, the following procedures are followed:

- The factor a is determined by measuring signals DC and r at room temperature, where the value of s is known to be negligibly small. Then a is calculated from

$$a = DC(room\ temp) / r(room\ temp) \,.$$

[2.10]

The a factor is an instrument-specific value that need only be determined once for a given set of gains of the lock-in and low-pass amplifier.

- r at room temperature is used to calibrate the system for absolute reflectance from the known room-temperature reflectance of the calibration wafer:

$$R_{fac} = R(room\,temp) / r(room\,temp) \,.$$

[2.11]

- The wafer is then heated to a temperature that is hot enough to yield a good signal-to-noise thermal emission signal, s_{cal}, yet cool enough to use the deposition system's thermocouple control temperature as a calibration value, T_{cal}, typically around 550 °C. Alternatively, the calibration may be made by observing the melting point of a Si/Al eutectic. The lock-in signal at the calibration temperature gives a value for $R_{cal} = R_{fac}\, r_{cal}$ at T_{cal}. Eqs. [1.15], [2.7], and [2.9] may then be used to calculate any surface temperature, given measured values for DC, r, DC_{cal} and r_{cal}:

$$\frac{1}{T} = \frac{1}{T_{cal}} - \frac{\lambda}{c_2} \ln \frac{(DC - ar)(1 - R_{cal})}{(DC_{cal} - ar_{cal})(1 - R_{fac} r)}.$$

[2.12]

The temperatures in Eq. [2.12] are in Kelvin. Eq. [2.12] is further simplified by lumping calibration constants into a single term and using Eqs. [2.7] and [2.9], yielding

$$\frac{1}{T} = \tau - \frac{\lambda}{c_2} \ln \frac{s}{(1 - R)},$$

[2.13]

where τ is given by:

$$\tau = \frac{1}{T_{cal}} - \frac{\lambda}{c_2} \ln \frac{(1 - R_{cal})}{s_{cal}}.$$

[2.14]

Eq. [2.13] is the expression used in a software implementation of the reflectance-correcting pyrometer. This calculation may be performed in less than a millisecond on virtually any computer.

2.3 *Temperature Overcompensation*

Fig 2.4 shows the results of one of the first tests of reflectance-corrected pyrometry obtained during the growth of a GaAs/ AlGaAs structure. The uncorrected waveform exhibits significant false temperature swings that track the measured reflectance interference oscillations.

The reflectance-corrected waveform shows considerable improvement over the uncorrected waveform, reducing the temperature artifacts from over 30° to 5°. However, the correction process appears to actually overcompensate for the effects of emissivity changes. The corrected waveform has oscillations that are out of phase with the uncorrected waveform. It is highly unlikely that the real surface temperature of the wafer oscillates at exactly the same frequency as the 900 nm thin film oscillations. Repeated tests of the pyrometer yielded consistent discrepancies, indicating that artifacts either in the analysis or in the instrument were present. This led to a series of studies to investigate the source of the artifacts and to seek a solution. The next section summarizes the results of these studies.

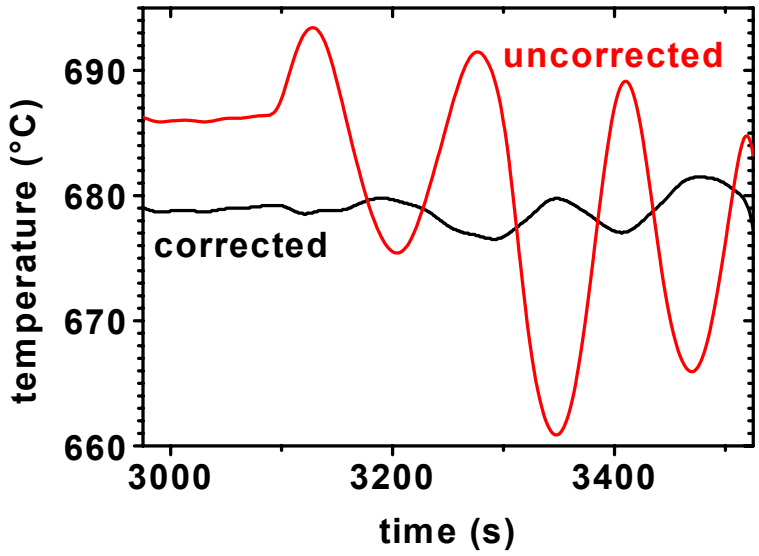

Fig 2.4: Results of reflectance-correcting pyrometry on a growing thin film structure. Top curve is Eq. [1.7] applied without reflectance corrections. Bottom curve results from the application of Eq. [2.13] using a measured reflectance signal. The large temperature swings seen in the uncorrected curve are due to changes in emissivity from thin film interference during growth. The corrected curve accounts for these emissivity changes, but appears to overcompensate the corrections.

3 Investigations of Pyrometer Errors

After encountering the overcompensation effects, the project was focussed on looking at how the pyrometer instrument was failing to yield the proper emissivity correction. Every aspect of the process became the subject of scrutiny. We reviewed the fundamental theory behind emissivity correcting pyrometry to ensure that the method was applicable to the steady-state, non-equilibrium process that exists during thin film growth. The assumptions leading to Eq. [1.14] were tested to ensure that they were valid during growth. Experimental artifacts arising from the finite range of angles and wavelengths used in gathering real signals were quantified. Errors in separating the reflectance and thermal emission signals due to electronic artifacts were explored. Detector spectral response and temperature coefficient effects were quantified. Artifacts from optical effects such as beam drift from wafer tilting, multiple reflections between optical components, and stray light effects were examined.

These studies revealed two significant sources that could lead to the observed temperature overcompensation effect: 1) errors in the measured absolute reflectance and 2) stray thermal emission that does not originate from the wafer surface. Of these two, the stray thermal emission contribution appears to be the largest effect. A correction scheme based on five sources of pyrometer errors is very effective at removing obvious artifacts in the temperature waveform (see 4.3). However, the absolute accuracy of the reflectance-correcting pyrometer is yet to be tested. We therefore consider it prudent to include summary discussions of all the potential sources for the overcompensation effect that were considered during the study. This section presents the results of the investigations.

3.1 Examination of Fundamentals

The section Fundamentals presents our careful re-examination of the fundamental applicability of emissivity-correcting pyrometry to the measurement of temperature during thin film growth. The method is completely sound, provided that the assumptions of opaque, smooth, flat, isotropic surfaces are met, and that an apparatus can be built to make accurate measurements of the terms contained in Eq. [1.15].

If the conditions $f(\lambda,\theta,\sigma) \cong F\ \delta(\lambda,\theta,\sigma)$ and $g(\lambda,\theta,\sigma) \cong G\ \delta(\lambda,\theta,\sigma)$ leading to Eq. [1.15] cannot be met, then a model-based least-squares fit of Eq. [1.14], combined with Eqs. [2.1] and [2.2] is required.

3.2 Validity of Assumptions

In this section, the three assumptions leading to Eq. [1.13] are reexamined to ensure that they apply to MOCVD growth conditions. We also question whether the presence of thin films could affect the applicability of Kirchhoff's law.

3.2.1 Opaque substrate

We have chosen a pyrometer wavelength of 900 nm as a good compromise between reasonable signal strength at temperatures near 500 °C and obtaining the best sensitivity at the shortest possible wavelength (Eq. [1.4]). GaAs has a bandgap near 850 nm, so the substrate is actually semi-transparent at room temperature. However, at 400 °C, the bandgap shifts to 1000 nm,

making the substrate opaque to 900 nm light. Room temperature reflectance measurements are accurate because there is no detectable thermal emission and negligible specular reflectance occurs off the rough backside surface of the wafer carrier after the light has passed through the polished vacuum/GaAs top surface. The pyrometer will *not* work for GaN on sapphire substrates, which is transparent to 900 nm light, even at 1100 °C.

3.2.2 Smooth, flat surface

If the wafer becomes rough during growth, the measured specular reflectance will be less than the correct hemispherical reflectance value, ρ, (see 1.5.2). Eq. [1.13] will therefore no longer be valid. The value for R will be small, leading to an overall overestimation of the actual surface temperature from Eq. [1.15]. Roughening also affects the total hemispherical emissivity (see Appendix A) which is responsible for heat transfer effects. In the limit of a very rough film, the emissivity will tend toward 1, thermal emission losses will be greater, and the surface temperature of the wafer will drop. Roughness also has complicated effects on the reflectance interference oscillations. High-reflectance parts of the oscillation are affected more by surface roughness than low-reflectance parts of the waveform. Because no clear interpretation of the effects of roughness could be made without modeling, measurements of surface roughness were made on wafers that exhibited temperature overcompensation during growth. The description of the experiment is detailed in Appendix B. The results of these measurements revealed that no significant surface roughening occurred during growth. The overcompensation effect must therefore arise from something other than surface roughening.

3.2.3 Isotropic reflectance

Reflectance anisotropy in compound semiconductors is a well-known effect. However, differences in reflectance due to azimuthal angle are negligibly small to be a factor in this application.

3.2.4 Presence of thin films

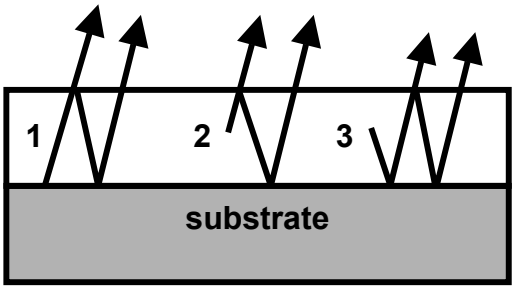

Fig 3.1: Three sources of thermal radiation for a hot opaque substrate with a semitransparent film on top. Radiation originates from 1) substrate 2) inside the film layer heading toward surface 3) inside film layer heading toward substrate. Radiation passing through the film is attenuated and undergoes multiple reflections at interfaces.

One may justifiably question whether the presence of semitransparent films on top of a substrate might affect the applicability of Kirchhoff's law. As illustrated in Fig 3.1, the presence of a film significantly complicates the thermal emission process. Emission may originate from the opaque

substrate and propagate through the film. If the film is absorbing, then radiation is also generated at every point within the film and propagates in all directions. In all cases, the radiation is attenuated and internally reflected as it makes its way to and out of the top surface. It may seem unlikely that these complicated radiation processes whose physical origins are inside the film could be described by the simple emissivity function $(1 - R)$, where R is just the external specular reflectance. Appendix C derives detailed expressions for the thermal emission sources illustrated in Fig. 3.1. The result is that when all sources of thermal emission are accounted for, the simple Kirchhoff's law expression is retained. In hindsight, this result should not be too surprising because Kirchhoff's law is derived from energy balance arguments that are independent of the details of the surface or the materials that comprise it.

3.3 *Errors in Signal Electronics*

An obvious source of artifacts in any experiment may come from non-linear behavior or defects in the signal measuring electronics. This source is less likely for our application because the same overcompensation behavior was observed with two different instruments using different signal gathering equipment and methods. Nonetheless, this obvious possibility needs to be tested.

There is one possible source of error in signal processing that can easily lead to artifacts in the temperature waveform regardless of the equipment used to collect it. The relationship in Eq. [1.13] assures us that the thermal emission signal, $s \propto \varepsilon \propto 1 - R$, will be exactly 180° out of phase with the reflectance signal, r. In any pyrometer instrument, s and r will be collected as raw signals with some smoothing filters applied to each signal. The smoothing filters will have characteristic phase-lag and time-constant responses. If these responses are not identical for each signal, the exact relationship between the shape and phase of s and r will become distorted. The distortion will in turn lead to artifacts in the temperature waveform extracted from the data. Because temperature extraction uses the ratio: s / $(1 - R)$, (Eq. [2.13]) small phase shifts in the waveform are amplified as derivative-like features. These features would have the same overall frequency as the reflectance oscillations. It is important, therefore to ensure that this is not causing the overcompensation effect.

In the specific case of the instrument shown in Fig. 2.3, it is critical to match the time response of the analog filter used to obtain the DC signal with the digital filter used in the commercial lock-in instrument. Appendix D provides details of this matching process.

3.3.1 Virtual reactor simulation

It was felt that the best way to thoroughly test all the electronics of the pyrometer system would be to synthesize a signal that simulates the raw $s + r$ voltage that would come from a detector mounted on a real reactor. This was done with the following procedure. First, a reflectance waveform was obtained from a computer program that calculates reflectance vs time for a growing thin-film structure. A DBR structure with a reflectance maximum at 900 nm was chosen because it provides a wide range of reflectance values to test the pyrometer. The waveform is shown in Fig. 3.2.

The reflectance waveform in Fig. 3.2 was used to calculate a thermal emission signal at 700 °C using Eq. [1.14]. A high-resolution digital representation of the combined thermal emission and

reflectance signals was then created. This was done by computing the values of each signal at 1 ms time intervals and adding the reflectance signal to the thermal emission signal in a way that simulated chopping at 100 Hz. The resulting waveform was stored as a large binary file on a computer. A program was then written to read this file and send a voltage out of a D/A converter at a 1 kHz rate according the values in the data file. This simulated the signal that would be received from a reflectance-correcting pyrometer detector monitoring the growth of the DBR. The signal was fed into the electronics of the pyrometer to determine if it could separate the thermal emission and reflectance signals and accurately back out the temperature. This performed a complete test of the electronics because the pyrometer instrument has no way of "knowing" that the input signal stream is synthetic.

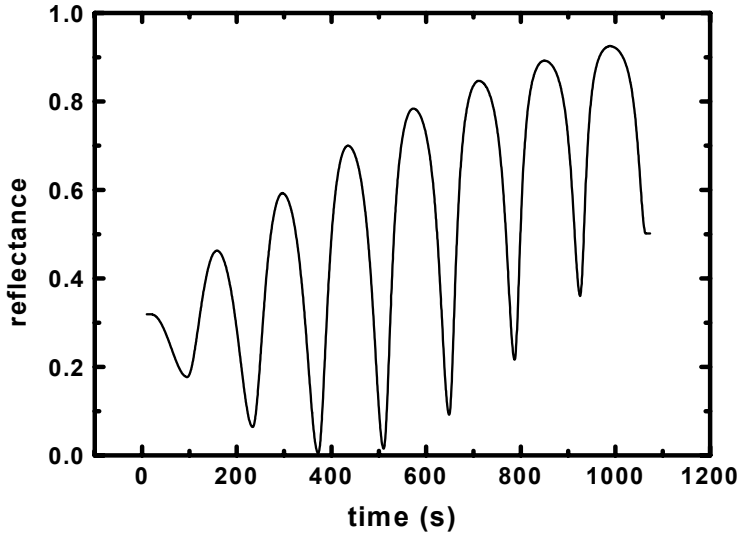

Fig 3.2: Calculated 900 nm reflectance waveform that tracks the growth of a GaAs/AlAs 900 nm DBR mirror on GaAs. Note that the reflectance of this structure has a broad range (from zero to 0.926) for testing the sensitivity of the reflectance-correcting pyrometer to all expected conditions.

The output of the pyrometer is shown in Fig. 3.3. Errors in the extracted temperature are less than 0.6 degrees, even at the highest reflectance value (0.926). They are caused by very small errors in the D/A and pyrometer electronics. Errors at the high reflectance values are expected to be nearly impossible to suppress (see 2.1.3). For reflectance values less than 0.7, the error is less than 0.1 °C. This simulation tests linearity, filter differences discussed above, the computer algorithm for extracting temperature, and all other electronics components in the pyrometer. The virtual pyrometer tests indicate that an undistorted signal will yield the correct temperature with the pyrometer shown in Fig. 2.3.

If the Analog and digital filters shown in Fig. 2.3 are purposely made different, the thermal emission signal is not exactly 180° out of phase with the reflectance signal and artifacts are generated. Fig. 3.4 shows the results of such a test. These artifacts are more symmetrically distributed about the correct temperature than the overcompensation effects seen in actual

experiments. The waveforms display phase-shifted derivative-type behavior to be expected from a mismatched time response in the electronics that distorts the waveform shapes.

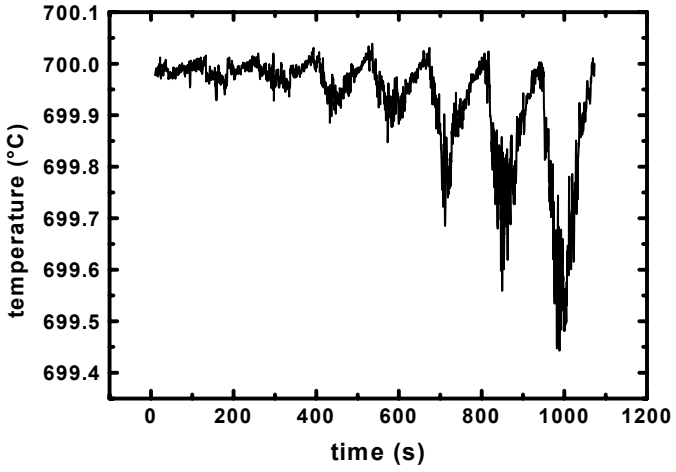

Fig 3.3: Temperature extracted by the pyrometer electronics from a synthesized signal. The signal was calculated for the 700 °C growth of a 900 nm DBR, whose reflectance waveform is shown in Fig. 3.2.

The results of the virtual pyrometer tests thus confirm that the electronics instrumentation is sound. However, an instrument that does not faithfully track the individual reflectance and thermal emission signals will produce artifacts. This possibility may be eliminated from consideration by performing virtual pyrometer tests.

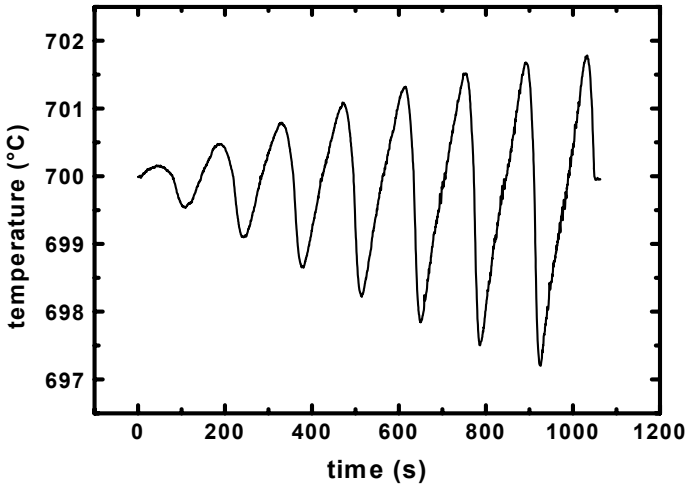

Fig 3.4: Temperature extracted by the pyrometer electronics from a synthesized signal. The analog filter used a 230 ms time constant and the digital filter was set to 690 ms. Different phase lags and response times distort the thermal emission and reflectance signals, causing artifacts in the extracted temperature.

3.4 *Overcompensation Caused by Reflectance Errors*

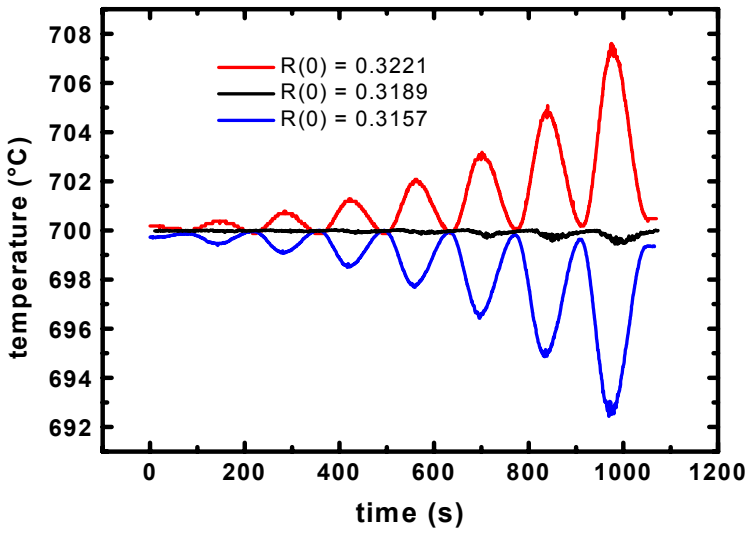

Fig. 3.5: Temperature extracted by the pyrometer electronics from the same synthesized signal using different starting reflectance calibrations. Top (red) curve used reflectance that was 1% high. Middle (black) curve used the correct value and is data shown in Fig. 3.3. Bottom (blue) curve used reflectance that was 1% low.

Overcompensation effects could be simulated in the virtual pyrometer experiments by using the wrong value for the starting reflectance, causing the wrong absolute reflectance value to be used in the temperature extraction. Fig. 3.5 shows the temperature profile obtained by using values of R_{fac} (Eq. [2.11]) that were 1% high and 1% low. Up to 7 °C errors were registered during the simulation for the highest (R = 0.926) reflectance values. The waveform shapes of these artifacts closely resemble those encountered in actual growth experiments.

The observed overcompensation effects yield an important result: Any errors in the absolute reflectance scaling during the experiment will give overcompensation behavior. The above result is a manifestation of the error analysis in 2.1.3. It is not enough that the two shapes of the reflectance and thermal emission signals be undistorted, but the reflectance calibration scaling must remain accurate throughout the run as well.

3.4.1 Analysis of reflectance error overcompensation

Eq. [1.15] reveals why the absolute value of the reflectance must be accurate. The reflectance appears in the expression as the ratio $s(1-R_{cal})/s_{cal}(1-R)$. Because R is being subtracted from 1, it is not possible to cancel calibration scaling errors with the above ratio. If R_{cal} is not accurate, it does not cause overcompensation artifacts because the constant value $(1 - R_{cal})$ is lumped into the τ factor in Eq. [2.14]. This will produce a systematic offset error for the temperature, but not time-dependent artifacts. However, if $R(t)$ is inaccurate, time-dependent artifacts will appear in the temperature waveform as incorrectly scaled values of R are subtracted from 1 and used in the above ratio.

This effect can be looked at from another point of view. The reflectance correction process is nothing more than dividing the thermal emission signal, *s*, which is proportional to $(1 - R)$, by a measured $(1 - R)$ to cancel out the emissivity factor. Nature always uses the correct value for *R* in the *s* signal, so it is up to the experimentalist to obtain the exact canceling factor $(1 - R)$ to make the correction work. Drift in *s* sensitivity doesn't affect this result because each term in the $(1 - R)$ factor in *s* is affected equally by the drift. Drift in *r* sensitivity causes a drift in *R*, but not in the constant factor, 1. This causes overcompensation artifacts.

An analytical expression for the temperature overcompensation effect may be derived from Eq. [2.13]. If the thermal emission and reflectance are measured perfectly, then the temperature is calculated from:

$$\frac{1}{T_{true}} = \tau - \frac{\lambda}{c_2} \ln \frac{s}{1 - R}.$$

[3.1]

Now assume that the thermal emission is measured perfectly, but the absolute reflectance is measured incorrectly, either because it was scaled wrong at the beginning of the experiment, or the sensitivity of the *r* signal drifts during the run. A simple parameterization of reflectance measurement errors is given by:

$$R_{\exp t} = \alpha R + \beta,$$

[3.2]

where α is a reflectance scaling error factor, and β is an offset error. A perfect measurement would have $\alpha = 1$ and $\beta = 0$. With measurement errors, Eq. [2.13] yields an incorrect value for the temperature that will have overcompensation effects, T_{ov}:

$$\frac{1}{T_{ov}} = \tau - \frac{\lambda}{c_2} \ln \frac{s}{1 - \alpha R - \beta}.$$

[3.3]

Provided that reflectance errors are small, $T_{ov} T_{true} \cong T_{true}^2$, one may combine Eqs. [3.1] and [3.3] to yield an expression for the value of the overcompensation difference, $T_{ov} - T_{true}$:

$$T_{ov} - T_{true} \cong \frac{\lambda T_{true}^2}{c_2} \ln \frac{1 - R}{1 - \alpha R - \beta}.$$

[3.4]

Eq. [3.4] illustrates the origin of overcompensation. If $\alpha = 1$ and $\beta = 0$, there is no error because the ratio in the ln term is 1. If $\alpha > 1$ and/or $\beta > 0$, the ln term is always greater than 1 and the overcompensation error is consistently positive. The magnitude of the error increases with

increasing R, creating artifacts that track the measured reflectance oscillations. A consistently negative error (which is actually an undercompensation) is produced for $\alpha < 1$ and/or $\beta < 0$.

Fig. 3.6 shows the overcompensation calculated from Eq. [3.4] for four different error conditions. As would be predicted by the analysis in 2.1.3, the overcompensation error grows without bounds as $R \rightarrow 1$. The data shown in Fig. 3.6 are consistent with the observed effects in Fig. 3.5. In particular, the overcompensation always stays either higher or lower than the correct value for the temperature for a given scaling or offset error. In the presence of obvious over(under)compensation as occurs in Fig. 3.5, therefore, the temperature associated with the lowest reflectance value is always the most accurate. The temperature is seen to reach the correct value when the DBR reflectance dips below 0.2, regardless of reflectance errors. It is clearly incorrect to average the temperature over several periods of overcompensation in an attempt to obtain the true temperature. If unavoidable errors in the reflectance are known to occur, it may be prudent to calculate the temperature as a weighted average using the weighting factor $(1- R)$ over the course of a reflectance oscillation.

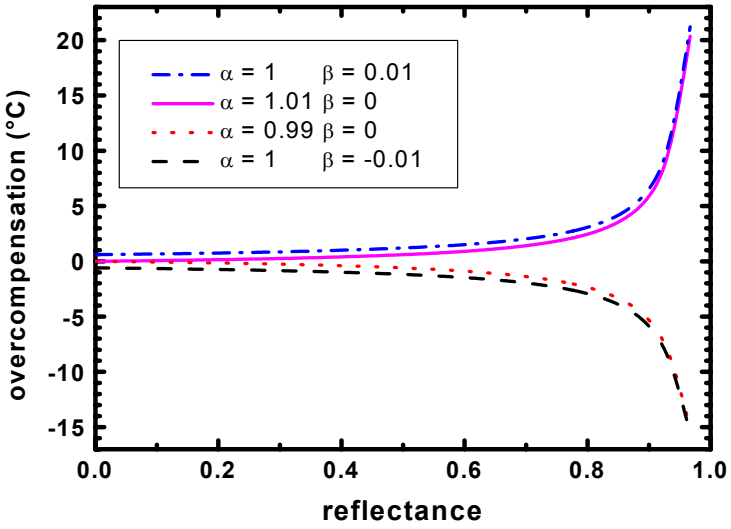

Fig 3.6: Temperature overcompensation calculated from Eq. [3.4] as a function of reflectance for four reflectance error conditions. T = 973 K (700 °C), λ = 900 nm.

Fig 3.6 implies that temperature measurements made when the reflectance is above 0.8 may not be trustworthy unless one knows that the reflectance is absolutely accurate to better than one percent. Unfortunately, many systematic errors in the apparatus can easily lead to reflectance calibration drifts of a few tenths of a percent during the run. Below is a summary discussion of some of the sources of these drifts.

3.5 *Sources of Reflectance Errors*

The virtual reactor simulations and the above analysis illustrate that small errors the absolute reflectance can lead to the temperature overcompensation effect. It is therefore important to

investigate situations in which the absolute reflectance can be affected both before and during the run. Some drifts during the run may be random, but others may be systematic, leading to a consistent overcompensation (or undercompensation) effect from run to run. We summarize these effects in terms of the analysis of section 3.4.1, above.

3.5.1 Signal offset (*beta*)

Because chopping and lock-in detection are being used to record the reflectance signal, *r*, in Fig. 2.3, offsets from the detector are eliminated. However, it is possible to obtain a chopped stray light signal from elements within the beamsplitter/lens/window assembly. Chopped light that is back-scattered into the detector before entering the MOCVD chamber will add a constant offset to *r*. Light scattered after returning from the wafer is proportional to *R* and will be accounted for in the self-calibration, producing no offset. Offset may by eliminated by careful optical design and by measuring the background lock-in signal with light going into the MOCVD chamber and no wafer in the wafer carrier. This background signal will remain relatively constant over many deposition runs if a stable light source is used. It therefore can be eliminated as part of the "*s*" calibration procedure (see 2.2.1).

3.5.2 Signal scaling error factor (*alpha*)

It is straightforward to eliminate reflectance signal offset, β, as outlined immediately above. Unfortunately, it is more difficult to control the signal scaling error factor, α. α may depart from 1 for a variety of static and dynamic reasons. If the wrong value of the starting absolute reflectance is used for determining R_{fac} in the run self-calibration, the behavior in Fig. 3.5 is observed. Even if the experiment starts out with the correct reflectance value, drifts in the detector sensitivity and systematic drifts in the opto-mechanical apparatus can affect the *r* signal, independent of the reflectance behavior of the wafer. It is also possible to have multiple reflections off the wafer and optics which add unexpected contributions to *r*. The remainder of section 3.5 deals with the sources of these variations in α.

3.5.3 Wafer starting reflectance.

The virtual pyrometer experiments point out the difficulties that one can encounter by using the wrong value for the wafer starting reflectance. This error creates an $\alpha \neq 1$ throughout the growth run.

There are two major sources for starting reflectance errors. First, the reflectance is temperature dependent. If the growth run is started with the wafer at a different temperature than that used for a literature value of *R*, then a calibration error will result. Fig. 3.6 shows literature values for the reflectance of GaAs at 900 nm as a function of temperature. The absolute accuracy of these data is not known, but is probably better than 1%. Fortunately, the temperature dependence of the reflectance is weak near room temperature ($\sim 7 \times 10^{-5}$ °C^{-1}), so no significant errors will be encountered if the MOCVD run is started with a wafer that is slightly above room temperature after being placed in an MOCVD chamber warmed from a previous run. However, if accurate values of the substrate reflectance as a function of temperature are available, they should be used in the starting reflectance calibration procedure. Other substrate materials may be more sensitive to starting temperature. There is very limited accurate data in the literature on these temperature effects.

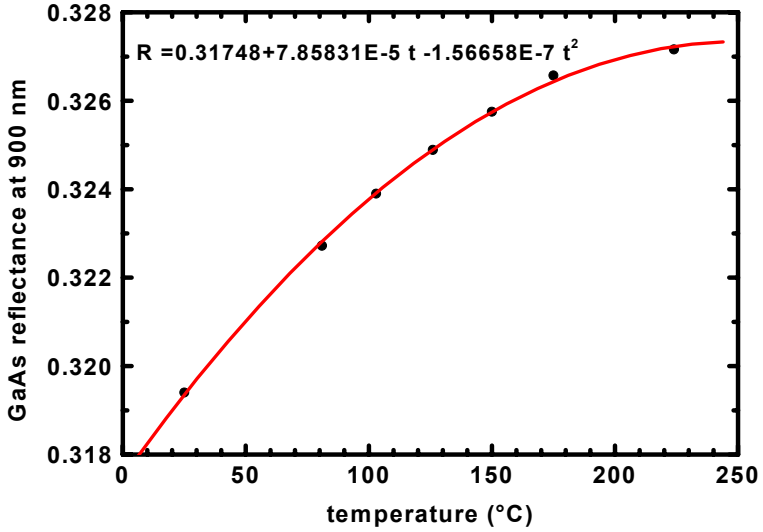

Fig. 3.6: GaAs reflectance as a function of temperature. (Data from C. H. Kuo, S. Anand, R. Droopad, K. Y. Choi, and G. N. Maracas, J. Vac. Sci. Technol. B 12 (1994) 1214, electronic version from G. N. Maracas). The fit may be used only over the temperature range shown.

The second starting reflectance error may arise from subtle, but significant effects of doping level on the substrate wafer reflectance. Fig. 3.7 shows room temperature absolute reflectance measurements on GaAs wafers using an apparatus similar to the one described by Strong[7].

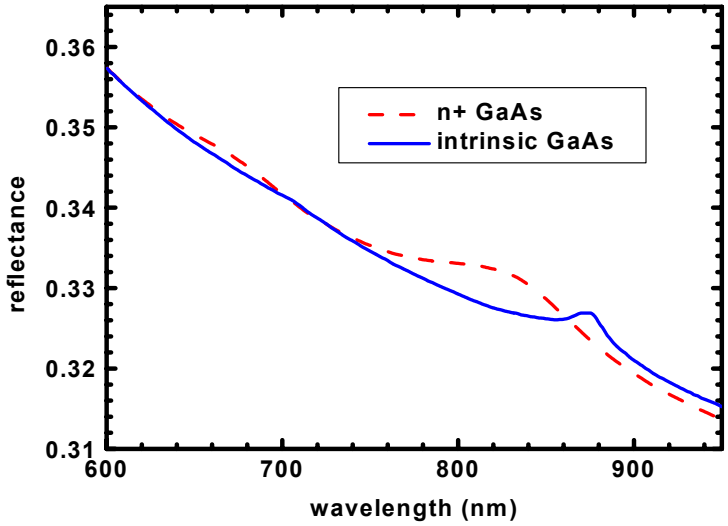

Fig 3.7: Measured absolute reflectance of GaAs, showing the differences in reflectance that are observed for different substrate doping levels.

Each curve is the average of five measurements. The precision of the measurements yields deviations of less than 0.001 reflectance units. Note that the reflectance near the bandgap is significantly affected by doping, emphasizing that accurate measurements of the actual wafer reflectance should be made for the best possible "*r*" calibration. For comparison purposes, the following reflectances are obtained for room temperature GaAs at 900 nm: 1) 23°C value from Fig. 3.6 formula: 0.31921, 2) intrinsic GaAs from Fig. 3.7: 0.32103, 3) n+ GaAs from Fig. 3.7: 0.31935. The difference between the literature value and the Strong measurement for intrinsic GaAs is 0.57%. The difference between the measured intrinsic and n+ substrates is 0.54%. Even these very small differences can lead to 3 °C overcompensation errors at $R = 0.9$.

3.5.4 Detector drift

Silicon PIN photodiodes are robust detectors. They are linear over at least 8 decades of signal strength and maintain their sensitivity (A / Watt of light) over many years without deterioration. As a result, they are often used in high-accuracy photometric instruments such as pyrometers and light meters for measuring absolute electromagnetic energy. The only significant source of sensitivity drift in a silicon detector is from environmental temperature effects.

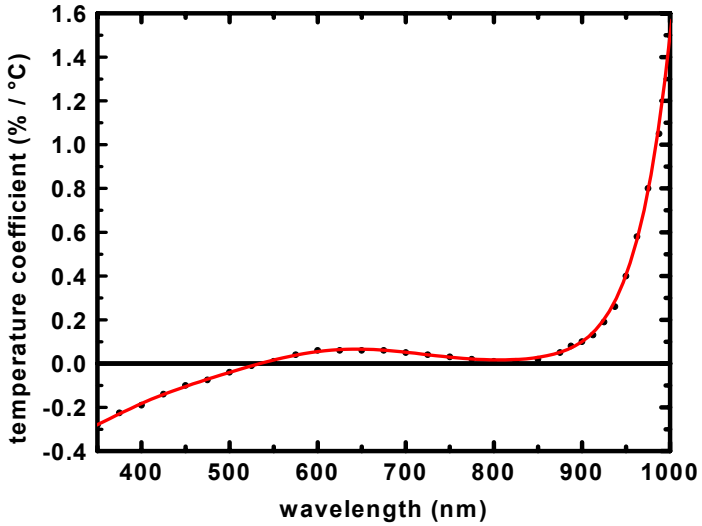

Fig 3.8: Temperature sensitivity of a silicon photodiode as a function of wavelength. (Data provided by UDT corporation).

Fig. 3.8 shows the temperature sensitivity of a silicon PIN photodiode. Wavelengths near 540 nm and 800 nm have practically no temperature sensitivity. At 900 nm, the response of the photodiode increases to 0.1 %/°C. Although this effect is relatively small, one must take steps to protect the detector from experiencing large temperature fluctuations during a run. This may be accomplished by placing the detector in an enclosure and controlling the temperature environment. Alternatively, active temperature compensation of the detector sensitivity may be employed. Long wavelengths near the silicon band edge are to be avoided for pyrometry applications because of the extreme temperature sensitivity.

3.5.5 Substrate tilt

Wafers are placed on a substrate holder in the MOCVD reactor. This holder is rotated at ~ 1000 RPM and heated to temperatures between 500 °C and 800 °C during deposition. Any tilt that the wafer experiences during this process will cause the reflected beam of light to be collected at an angle different than the exact normal. It is very difficult to design an optical system that provides an unaltered signal for all tilt angles. Fig. 3.9 shows a plot of signal vs. tilt angle for the pyrometer beamsplitter probe (shown schematically in Fig 2.3). High-frequency wobble caused by wafer rotation is not a problem because it can be averaged to a mean signal. However, it is possible that as the wafer is heated from room temperature to the deposition temperature, thermal expansion and mechanical stresses cause the overall wafer holder to creep to a new average tilt position. Fig. 3.9 indicates that if this average tilt exceeds 0.2° in some directions, more than a 1% drift in the signal sensitivity will occur. This will produce reflectance scaling factor errors and overcompensation effects.

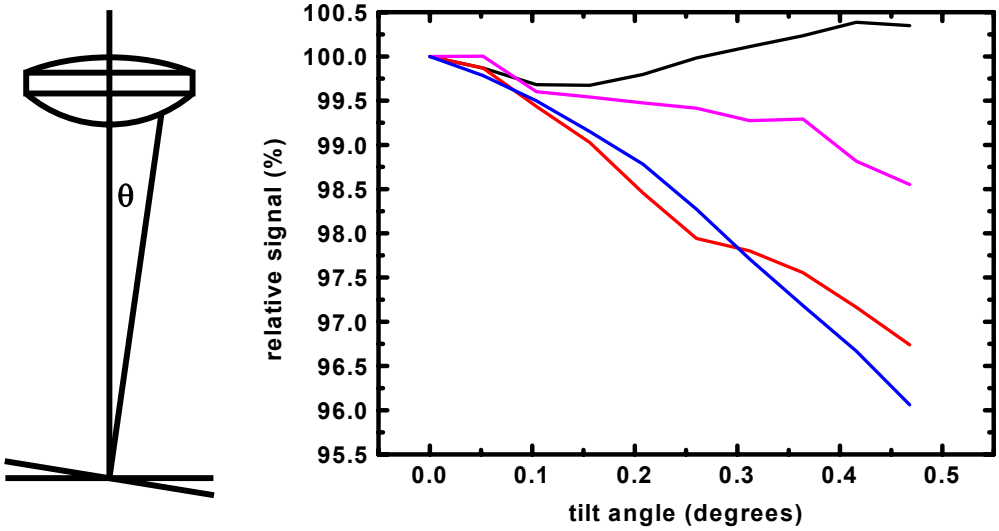

Fig 3.9: Variation in reflected light signal from the beamsplitter probe shown in Fig. 2.3 as a function of wafer tilt angle, θ. Data is for a tilt in both directions from the normal in each of two orthogonal planes.

It is very difficult to construct an optical probe that is completely immune to wafer tilt. Modeling of the probe using lens design software reveals that subtle effects from Fresnel reflections off the beamsplitter is the primary cause of the tilt sensitivity shown in Fig. 3.9. This sensitivity may be reduced at a cost of more complex optical design.

3.5.6 Wafer-to-lens distance drifts

The optical probe is also sensitive to changes in the vertical distance between the collecting lens and the wafer. The beamsplitter probe has a measured sensitivity of 0.2%/mm for the reflectance signal. As the MOCVD system is brought up to deposition temperature, thermal expansion of the wafer holder will slightly reduce the lens-to-wafer distance. This reduction can lead to scaling factor errors for a reflectance signal that is calibrated at room temperature.

3.5.7 Multiple reflections from ghost rays

If the window for the reactor is not anti-reflection (AR) coated, it is possible for the reflectance monitor to receive an extra signal from "ghost rays", as illustrated in Fig. 3.10:

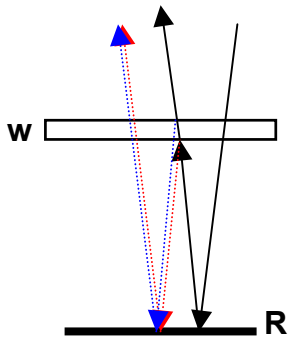

Fig 3.10: "Ghost ray" reflections from the window in the MOCVD reactor can add to the reflectance signal. Pictured are two of many possible ghost rays. One ray reflects off the bottom surface of the window, hits the wafer, and then passes to the detector. The second ray reflects off the inside of the top surface of the window. Because the ghost rays bounce more than once from the wafer, their contribution is not simply proportional to the wafer reflectance. This causes scaling errors.

This figure shows only two of many possible ghost rays from all the optical components in the probe that could contribute to the reflectance signal. If the reflectance from each surface of the window is given by w, then the transmission through each window surface is $(1 - w)$, and the following signals are obtained:

$$\begin{aligned} &main\ signal : R(1-w)^2 \\ &1^{st}\ ghost : RwR(1-w)^2 \\ &2^{nd}\ ghost : R(1-w)w(1-w)R(1-w)^2 \end{aligned}$$

[3.5]

Both ghost signals contain factors that contribute to a scaling error, $\alpha = 1 + Rw + Rw(1-w)^2$, in the total reflectance signal. For a single uncoated surface, $w \cong 4\%$. However, geometrical constraints on the optical setup determine how much of the ghost ray actually reaches the detector, so it is difficult to determine the magnitude of the error without a detailed ray tracing model of the entire reflectance probe. Ghost ray effects cause two problems. The reflectance is not scaled correctly at the beginning of the run, and the value of α will vary during the run, depending on the value of the wafer reflectance. Ghost ray effects may be minimized by AR coating all optical components and by using an arrangement that rejects light that does not pass through an image of the detector fiber placed directly on the wafer (see Appendix E).

3.6 Overcompensation from Emission Signal Errors

As pointed out in section 3.4.1, reflectance-correcting pyrometry will work provided that the ε = (1 – R) factor imbedded in the thermal emission signal is divided out by a correctly measured (1

– R) factor obtained from a reflectance measurement. Improper scaling of the thermal emission signal will not lead to overcompensation artifacts because the overall waveform of the emission signal will still contain a (1 – R) factor determined by the physics of the thermal emission process. However, it is possible to distort the thermal emission signal such that the (1 – R) factor is not exactly cancelled. This section outlines the sources of such distortions.

3.6.1 Analysis of emission signal overcompensation

Following the same line of reasoning as 3.4.1, we start with the expression for the exact temperature (Eq. [2.13]):

$$\frac{1}{T_{true}} = \tau - \frac{\lambda}{c_2} \ln \frac{s}{1-R}$$

[3.6]

We then parameterize errors in the measurement of s with scaling and offset error terms:

$$s_{\exp t} = \delta s + \tilde{\gamma}$$

[3.7]

The above expression does not reveal the explicit dependence of s on reflectance, given by Kirchhoff's law. A more insightful parameterization takes advantage of this fact:

$$s_{\exp t} = \delta(1-R)L_b(T_{true}) + \tilde{\gamma}L_b(T_\gamma)$$
$$\frac{1}{T_{ov}} = \tau - \frac{\lambda}{c_2} \ln \frac{\delta(1-R)L_b(T_{true}) + \tilde{\gamma}L_b(T_\gamma)}{1-R}$$

[3.8]

The offset term, $\tilde{\gamma}$, is associated with blackbody thermal emission from some non-wafer source, such as the wafer carrier, and contains no explicit reflectance terms. We allow for the possibility that the wafer carrier may be at a different temperature than the surface temperature of the wafer, i.e. T_{true} may or may not be equal to T_γ. We are assuming that trivial electronic offsets for s may be eliminated, leaving the $\tilde{\gamma}$ factor to deal only with stray signals from a thermal source. $\tilde{\gamma}$ is thus always ≥ 0.

With the above error parameterization, the expression for temperature overcompensation from emission signal errors is:

$$T_{ov} - T_{true} \cong \frac{\lambda T_{true}^2}{c_2} \ln \frac{\delta(1-R) + \tilde{\gamma}L_b(T_\gamma)/L_b(T_{true})}{(1-R)}$$

[3.9]

Fig. 3.11 shows the overcompensation calculated from Eq. [3.9] for three different error conditions. As expected, scaling errors from δ produce relatively small errors in the temperature

that are not a function of the reflectance. These errors will not track the reflectance waveform to produce oscillatory artifacts. However, the offset error generated by $\tilde{\gamma}$ does give an overcompensation effect that produces essentially the same waveform as is produced from reflectance errors. The effects are so similar, in fact, that it is difficult to determine exclusively from a temperature overcompensation waveform whether the deviation is due to reflectance scaling errors or emission signal offset errors. Checking the emission signal for offsets at high

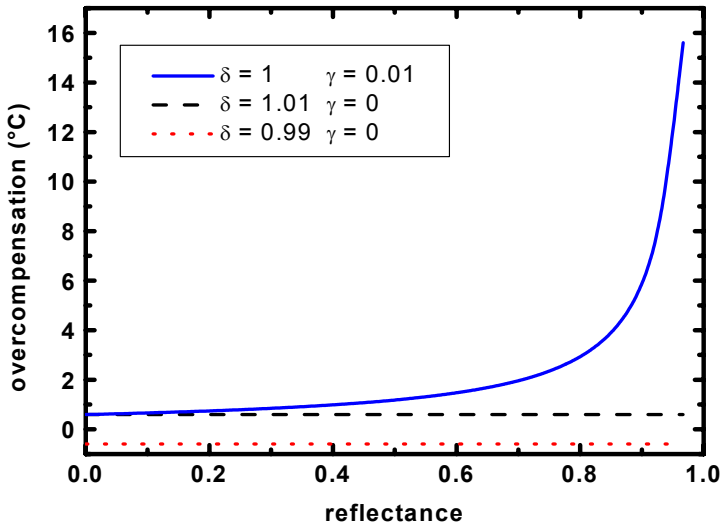

reflectance values will partially resolve this issue (see sec 4.2).

Fig. 3.11: Temperature overcompensation calculated from Eq. [3.9] as a function of reflectance for three error conditions. T_{true} = 973 K (700 °C), λ = 900 nm. T_γ is assumed to be equal to T_{true} in this plot.

3.7 ***Sources of Emission Signal Errors***

Given that emission signal errors are also capable of creating overcompensation artifacts, we consider below the sources of such errors. The error sources in this section give a thermal radiation measurement that is the desired signal plus two background signals:

$$s = C\delta(1-R)L_b + \tilde{\gamma}L_b + \zeta R L_b \qquad \textbf{[3.10]}$$

The error parameter δ describes a systematic scaling error in the thermal emission signal from the wafer. The error parameter $\tilde{\gamma}$ accounts for the emissivity of the wafer carrier and all geometric effects determining how much stray light reaches the detector. We also introduce an additional offset error factor ζ that accounts for stray radiation that has reflected once off the wafer prior to detection. For simplicity, we assume that the wafer carrier is at the same temperature as the wafer. Below are descriptions of the physical sources of these errors.

3.7.1 Signal scaling error (delta)

As seen in Fig. 3.11 above, a scaling error does not lead to overcompensation artifacts, but can cause a fixed, systematic error in the temperature. As revealed in sec 2.1.3, the temperature errors are not highly sensitive to scaling errors. Moreover, the emission signal is much less prone to scaling errors in the first place. The wafer acts as an almost diffuse source of thermal emission in the near-normal direction. Light from this source is collected by the full solid angle of the collection optics. In contrast to the reflectance measurement, tilt of the wafer and wafer-to-lens variations have a negligible effect on the emission signal sensitivity. Detector sensitivity drift thus becomes the only viable factor in scaling errors.

3.7.2 Multiple reflections from ghost rays

As with reflectance errors, the presence of ghost rays discussed in 3.5.7 can possibly add artifacts to the thermal emission signal. Thermal radiation that emanates from the surface of the wafer may undergo multiple reflections from optical surfaces of the probe and add to the thermal emission signal. Using the simple two-ghost-ray example from 3.5.7, we would have $\delta = 1 + Rw + Rw(1-w)^2$. Because δ contains reflectance terms, overcompensation artifacts are to be expected.

3.7.3 Signal offset (gamma)

It is possible for stray light to reach the detector from hot surfaces that do not hold wafers. If such signals contaminate the thermal emission, then the reflectance correction scheme will not be completely effective because the stray light contains no (1 – R) factor.

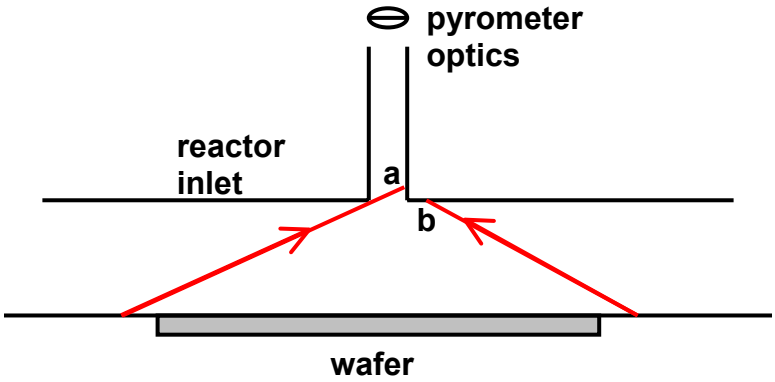

Fig 3.12: Possible sources of stray thermal emission from the wafer carrier. **a)** Light strikes the rough surface of the optical access tube and subsequently illuminates the pyrometer optics ($\tilde{\gamma}$ contribution). **b)** Light strikes the rough surface at the bottom of the inlet. This acts as a virtual source of stray radiation when it is reflected off the wafer and back into the pyrometer optics (ζ contribution).

Fig 3.12 shows how thermal emission from the wafer carrier can reach surfaces that may act as diffuse secondary sources for stray light contamination. Contributions from these sources may be minimized by careful optical design. Specifically, the end of the optical fiber that goes to the detector may be imaged directly on the wafer by the pyrometer collection optics. With this configuration, marginal rays from the collection lens never intersect the walls of the inlet optical access tube. The secondary sources along the tube thus cannot be "seen" by the detector.

3.7.4 Reflected signal offset (zeta)

One must also ensure that marginal rays reflected off the wafer do not intersect the surfaces labeled by **b** or **a**. If intersection occurs, these surfaces will act as remote, out-of-focus diffuse virtual sources reflected from the wafer. These sources will contribute $\zeta R L_b$ to the thermal emission signal error. This contribution is largest at the largest values for R, and where the pyrometry algorithm is most sensitive to errors. Powers of R are also possible with multiple wafer reflections within the reactor.

Appendix E provides more details on the optics of stray thermal emission sources and the spatial filtering steps that can be taken to minimize these errors.

4 Correcting Pyrometer Errors

Section **3** outlines the sources of errors in the reflectance-correcting pyrometer and suggests ways to minimize their effects. Despite efforts to eliminate all such errors, our experiments with a prototype pyrometer still yielded temperature overcompensation artifacts. This section describes how software solutions were used to largely eliminate the artifacts by effectively measuring and compensating for the errors as part of the calibration process.

4.1 900 nm DBR Test Structure

The virtual reactor tests outlined in section 3.3.1 used a 900 nm DBR mirror stack structure to create a wide variety of reflectance values over which to test the reflectance-correcting pyrometer algorithms. Such a structure is also useful for testing real pyrometer systems. Because the optical constants of compound semiconductors are temperature dependent, a DBR structure designed for a maximum room-temperature reflectance of ~850 nm will shift to a reflectance maximum near 900 nm at MOCVD growth temperatures.

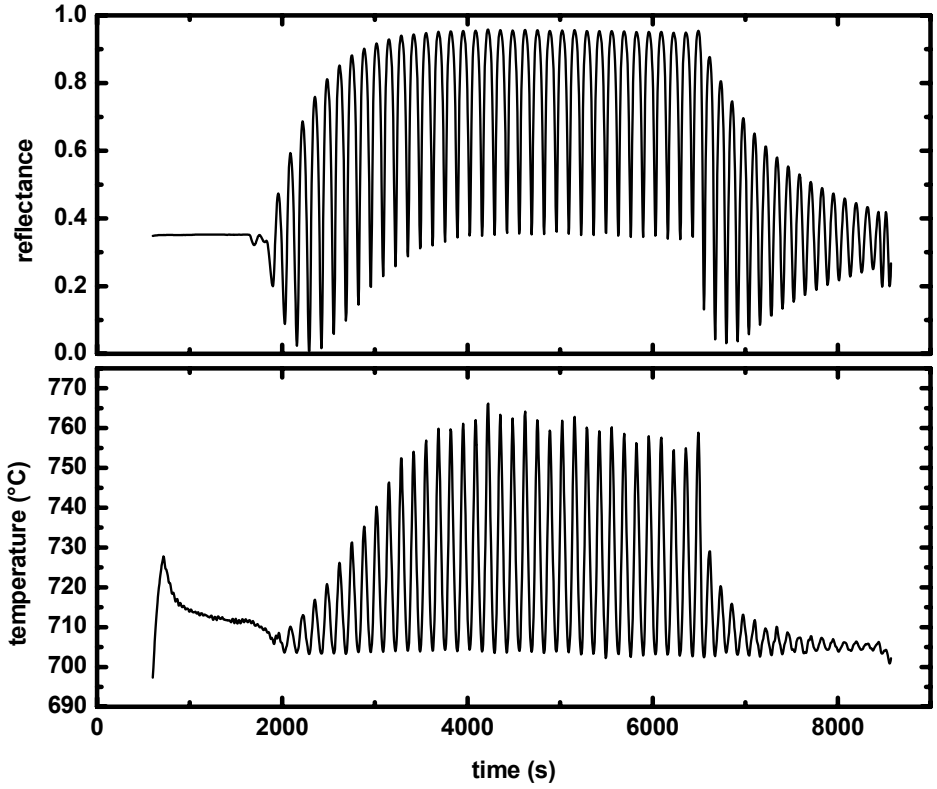

Fig 4.1: Temperature (lower curve) and reflectance (upper curve) extracted from a reflectance-correcting pyrometer during the growth of a 860 nm optically pumped VCSEL structure. Large temperature overcompensation effects are observed when the reflectance is greater than 0.7.

Fig. 4.1 shows the temperature and the reflectance from a 860 nm optically pumped vertical-cavity surface emitting laser (OP-VCSEL) structure. The structure producing the lower mirror

was 1200 Å of 20% AlGaAs followed by 35 stacks of 615 Å 16% AlGaAs | 720 Å AlAs. The mirror has its reflectance maximum near 900 nm at the growth temperature of ~700 °C, providing a wide range of reflectance values with which to test the reflectance-correcting pyrometer. Very large temperature overcompensation effects are evident. The artifacts are greatest at high reflectance values and look similar in appearance to that predicted in Fig 3.5. in section 3.4.

From the analysis of pyrometer errors in section **3**, we may conclude that we have either systematic reflectance errors in the form of scaling (α), and/or offset (β), and/or that we have thermal emission offset signals ($\tilde{\gamma}$) and (ζ). Scaling errors in the thermal emission (δ) is also possible, but is less obvious because it does not yield oscillatory waveforms. One way to account for these errors is to measure them and construct new pyrometry model functions from Eqs. [3.3] and [3.8].

4.2 *Physical Origin of Observed Errors*

Reflectance scaling errors, α, could be used to simulate the observed overcompensation, but the values of α that were required to match the observation were unreasonably large. The reflectance scaling would need to be off by at least ten percent to achieve the observed artifacts. Such scaling errors are not reasonable for the beamsplitter probe used in our instrument. Experiments using 900 nm AR coatings on windows and lenses were used to test for multiple-reflection, ghost-ray effects. No strong evidence for these effects was found. Examination of the thermal emission signal revealed that offsets from $\tilde{\gamma}$ and/or ζ factors were most likely the major cause of overcompensation artifacts.

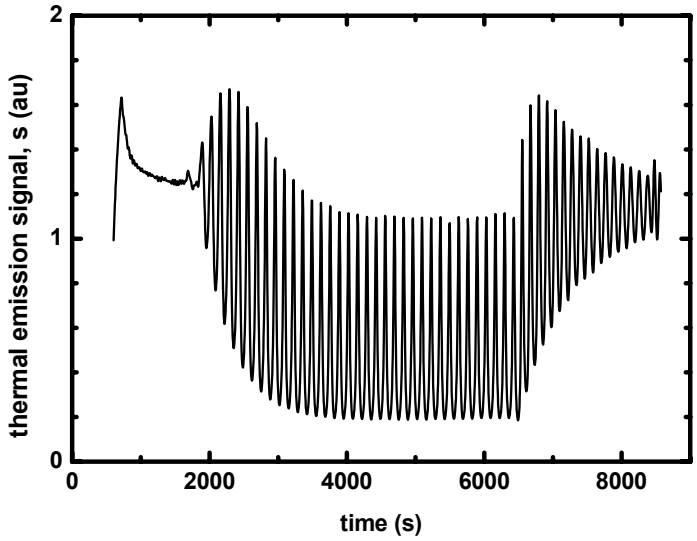

Fig 4.2: Thermal emission signal for the 860 VCSEL structure in Fig. 4.1.

Fig. 4.2 shows the thermal emission signal for the 860nm OP-VCSEL structure described above. As expected, the signal is 180° out of phase with the reflectance signal, Fig 4.1. However, as the reflectance approaches 1, the thermal emission signal is seen to not approach zero, as Kirchhoff's

law would dictate. This is strong evidence that stray light from the wafer carrier is adding an offset to the thermal emission signal. This offset is clearly thermal in nature because it disappears when the system is cooled to room temperature. It is not possible to determine whether $\tilde{\gamma}$ or ζ factors are dominating at high reflectance values.

As the next section shows, it is virtually impossible to separate out any of the five error factors from any experimental data. The effects of all factors reduce to a single universal error parameter.

4.3 *The Gamma Factor as a Universal Correction*

Given that we wish to eliminate artifacts and not actually individually measure each error factor introduced above, we can account for all factors, yet describe their effects using just a single parameter. Solving for R in Eq. [3.2] and substituting into Eq. [3.10] we obtain

$$s = \frac{c_{1L}}{\lambda^5}\left[C\delta\left(1-\frac{R_{\exp t}-\beta}{\alpha}\right)+\tilde{\gamma}+\zeta\frac{R_{\exp t}-\beta}{\alpha}\right]e^{-c_2/\lambda T}$$

[4.1]

All the terms inside the square brackets reduce either to constants or to first-order coefficients of R_{expt}. After summing all constants and factoring out the R_{expt} coefficient , Eq. [4.1] may be re-written in the equivalent form:

$$s = F\left(1-R_{\exp t}+\gamma\right)e^{-c_2/\lambda T}$$

[4.2]

where we use γ without the tilde as an "effective thermal radiation" offset term. Despite the inclusion of five error factors describing five different physical phenomena, the linear functional form of the pre-exponential in Eq. [4.1] allows for only two mathematically unique numbers. One of these, F, will be eliminated during self-calibration. All details leading to overcompensation effects are thus mathematically lumped into only a single universal parameter, γ, that cannot be further dissected to extract the original error parameters. In fact, linear contributions from ghost rays will also be accounted for in this formalism. This mathematical "lumping" of parameters presents a serious difficulty if one wants to measure individual error contributions. From an empirical point of view, however, we are fortunate to have to fit only one parameter in order to rigorously account for all five error factors.

4.3.1 New reflectance-correcting pyrometer equation

By eliminating the constant F with an *in-situ* calibration measurement, we obtain a new reflectance-correcting pyrometry equation that simultaneously can correct for all systematic errors in the reflectance and stray thermal emission from the wafer carrier:

$$\frac{1}{T} = \frac{1}{T_{cal}} - \frac{\lambda}{c_2}\ln\frac{s\left(1 - R_{exp\,t}^{cal} + \gamma\right)}{s_{cal}\left(1 - R_{exp\,t} + \gamma\right)} = \tau - \frac{\lambda}{c_2}\ln\frac{s}{1 - R_{exp\,t} + \gamma}$$

$$\tau = \frac{1}{T_{cal}} - \frac{\lambda}{c_2}\ln\frac{1 - R_{exp\,t}^{cal} + \gamma}{s_{cal}}$$

[4.3]

Although the constant $(1+\gamma)$ could have been written as a single variable, we choose to retain the original functional form of Eq. [2.13] with γ collectively accounting for all the above errors; i.e. if γ is zero and there are no reflectance scaling and offset errors, then Eq. [2.13] is restored. The parameter γ may be viewed as an "effective thermal emission offset", or, more precisely, a universal correction parameter for all first-order offsets and scaling errors.

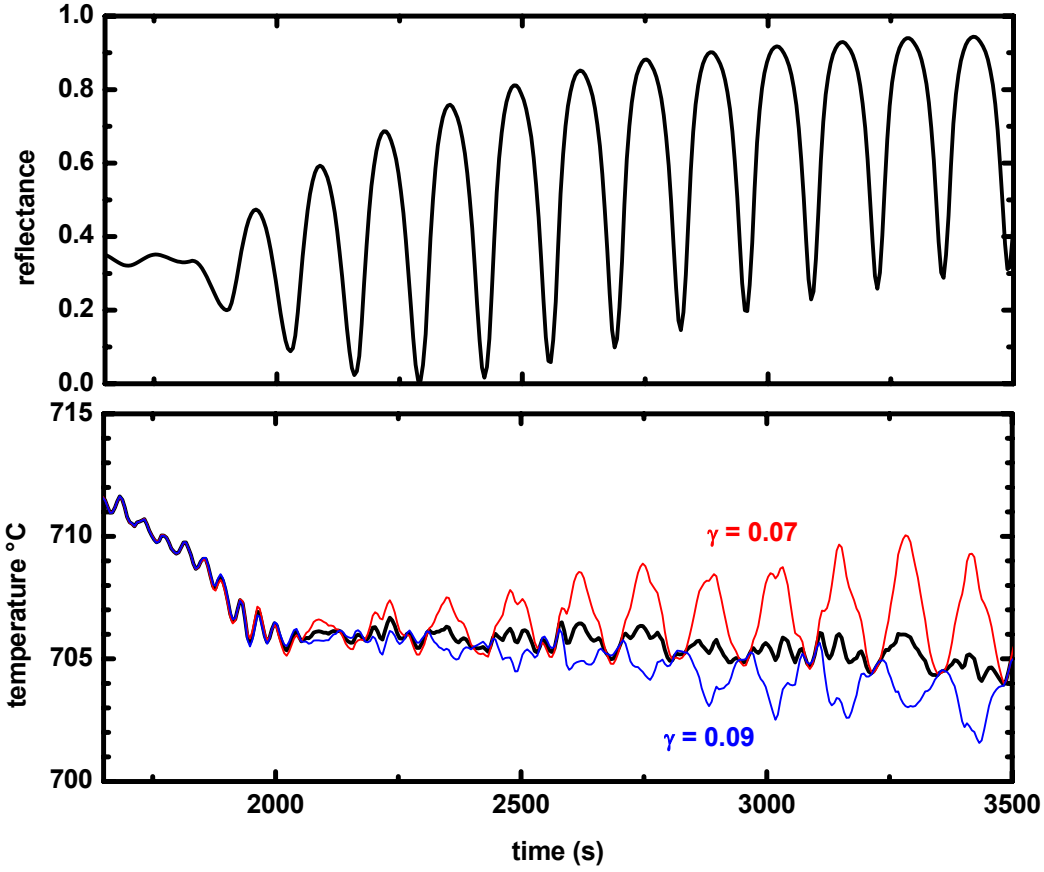

Fig 4.3: Effect of applying the γ factor in Eq. [4.3] to the data of Figs. 4.1 and 4.2. γ = 0.07 gives overcompensation (upper red curve). γ = 0.09 gives undercompensation (lower blue curve). Minimum-variance fit, γ = 0.081 minimizes artifacts (middle black curve).

4.3.2 Effect of gamma on experimental data

Fig 4.3 shows the effects of using γ on the DBR data shown in Figs. 4.1 and 4.2. In each case, a fixed value of γ was used in Eq. [4.3] to extract the temperature. As expected, the effects of γ are most readily seen at high reflectance values. Very little difference between the choice of γ = 0.07, 0.08, or 0.09 is evident for reflectance values below 0.6. This figure illustrates why the choice of a DBR structure is ideal for determining γ. Over each high-low index stack, the reflectance varies over a wide range. A minimum-variance fit (see Appendix F for derivation) over this wide range yields an optimal value for γ that is effective at suppressing artifacts for virtually any subsequent deposition. With the optimum choice of γ = 0.081, noise and residual temperature oscillations are reduced to a peak-to-peak value of only 2 °C. This is a substantial improvement over the 60 °C peak-to-peak artifacts exhibited in the γ = 0 temperature waveform in Fig. 4.1.

4.3.3 Effect of an optimized gamma

The γ factor is determined by a minimum-variance fit to thermal emission data taken over a wide range of reflectance values and at a fixed temperature whose actual value does not need to be known. Appendix F derives the formulas used for determining γ. A convenient choice for γ determination is a DBR structure with a reflectance maximum at 900 nm, such as the one described above. It provides reflectance values ranging between zero and above 0.9. It is important that the surface temperature remain fixed during the DBR growth in order to obtain an accurate γ factor. Appendix G shows that the assumption of constant average temperature required to extract γ is warranted, provided that an initial transient section at the beginning of the DBR growth is avoided.

If γ is known, and a calibration run is performed, Eq. [4.3] may be used to extract an accurate temperature from a measured s and R, even if any of the five linear errors is present. Note that the processes of determining γ and calibration are completely separate activities. A calibration to measure s_{cal} and R_{cal} may be made without knowing the value of γ. Once γ is determined, then τ may be calculated and Eq. [4.3] used to extract temperatures.

Fig. 4.4 shows the complete temperature waveform during the growth of the 860 nm OP-VCSEL structure. Once the overcompensation artifacts that dominate the waveform in Fig 4.1 have been removed, one can see interesting variations in the surface temperature during the growth. The initial heating of the wafer is followed by a 5° drop during the growth of the 1200 Å AlGaAs layer. This drop is due to the overall increase in the total surface emissivity from the AlGaAs layer, which causes higher radiative losses (see Appendix A for discussion). The temperature during the growth of the DBR is relatively constant, but shows a gradual 3° drop over the 1:15 h deposition time. After the DBR growth ends at 6500 s, the temperature changes abruptly by several degrees as 1155 Å layers of 20% AlGaAs are placed on top of the DBR.

Fig 4.5 shows the application of a DBR-determined γ factor to a subsequent MOCVD growth run. This is a simple two-layer structure consisting of 200 nm of AlAs followed by 220 nm of GaAs. Note that the gamma corrected waveform shows no obvious overcompensation artifacts. The temperature changes that remain after reflectance and gamma corrections are consistent with

a temperature drop as the higher-emissivity AlAs is grown, followed by a recovery during lower emissivity GaAs growth.

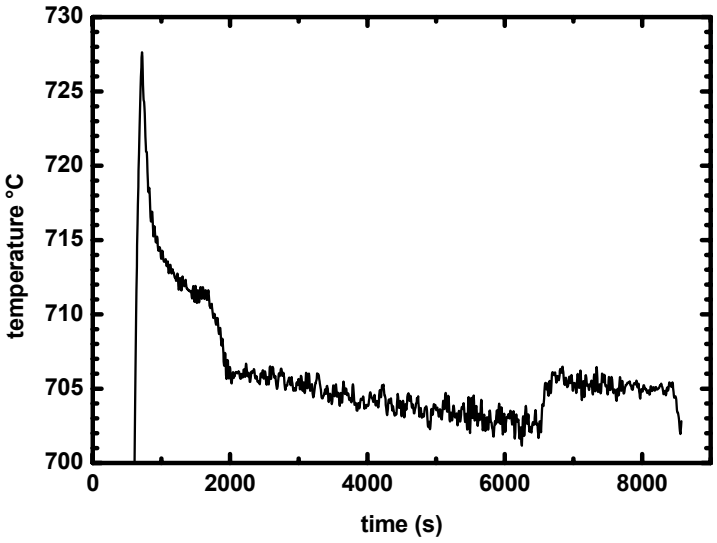

Fig 4.4: Temperature extracted with Eq [4.3] using γ = 0.081 for the OP-VCSEL structure first shown in Fig. 4.1.

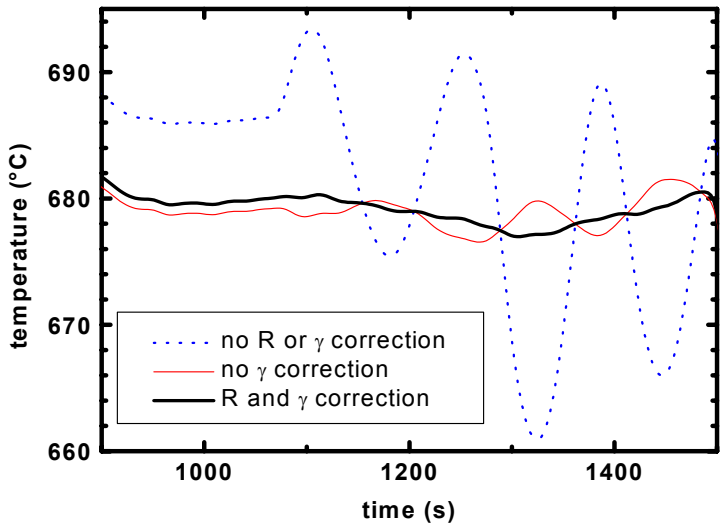

Fig 4.5: Temperature during the growth of 200 nm of AlAs followed by 220 nm of GaAs. Gamma correction removes temperature overcompensation artifacts.

Fig 4.6 shows a waveform for the two-layer structure grown at four different thermocouple setpoint values: 750, 700, 640, and 580 °C. Note that the surface temperature as measured by reflectance-correcting pyrometry systematically departs from the setpoint value as the temperature is increased. This is a consequence of the increased role that radiative losses play in

the steady-state temperature (see Appendix A). It is also an experimental verification that the heater controller cannot detect all the temperature changes that are occurring at the wafer surface.

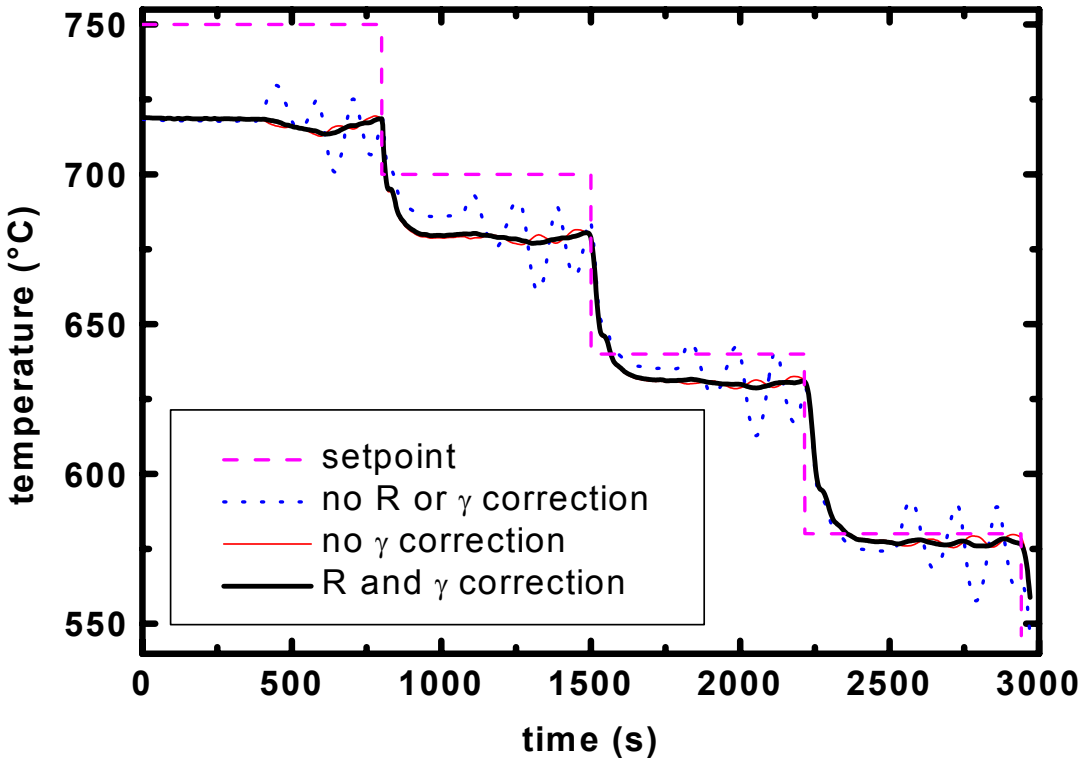

Fig 4.6: Temperature waveforms during the growth of a 200 nm AlAs / 220 nm GaAs structure at four thermocouple setpoint temperatures.

Also note that the temperature changes during deposition are smaller at lower temperatures, consistent with the fact that radiative losses are less important at lower temperatures.

Some artifacts appear at the lowest (580 °C) setpoint value. This may be an indication that the errors measured by the γ factor are not constant for all temperatures.

4.3.4 Accuracy of reflectance-correcting pyrometry

Figs 4.4 – 4.6 clearly show the advantages of applying the γ factor to the reflectance correcting pyrometry equation. It is difficult to determine whether this correction maintains absolute accuracy. Unfortunately, instrumented wafer experiments planned to test for absolute accuracy were not performed because Sandia's research reactor had a catastrophic heater failure. Such measurements can only be done in a reactor that does not spin the wafer and can survive a drastic change in conditions without coating critical parts of the reactor.

Appendix F presents two methods for the determination of γ. We prefer to use the minimum-variance method, coupled with in-situ calibration. This method has the benefit of being theoretically accurate, provided that all calibrations are correct and that the γ factor is representative of all constant systematic errors.

Growth runs performed on Sandia's EMCORE D125 reactor have shown that reflectance-correcting pyrometry measurements provide consistent, reproducible results even after multiple temperature calibrations. Because consistency is usually sufficient for MOCVD growth, the pyrometer has become a valuable tool and is used routinely for all growth runs. Absolute accuracy is therefore not as important in MOCVD device fabrication applications as it would be for fundamental research.

5 Measurements on Multiple Wafers

The pyrometer data shown thus far has been obtained on a single-wafer MOCVD reactor. Larger commercial systems employ multiple wafer systems in which the pyrometer unavoidably views parts of the wafer carrier in the gaps between wafers. Given that it is necessary to account for stray thermal emission with the γ factor correction, a thermal emission signal that includes part of the wafer carrier for part of the rotating disk cycle could still use Eq. [4.3] to extract temperature. One would expect a larger γ, but the wafer temperature should still be measurable. Reflectance from the wafer carrier is negligibly small, so the correction is a nearly pure $\tilde{\gamma}$ contribution.

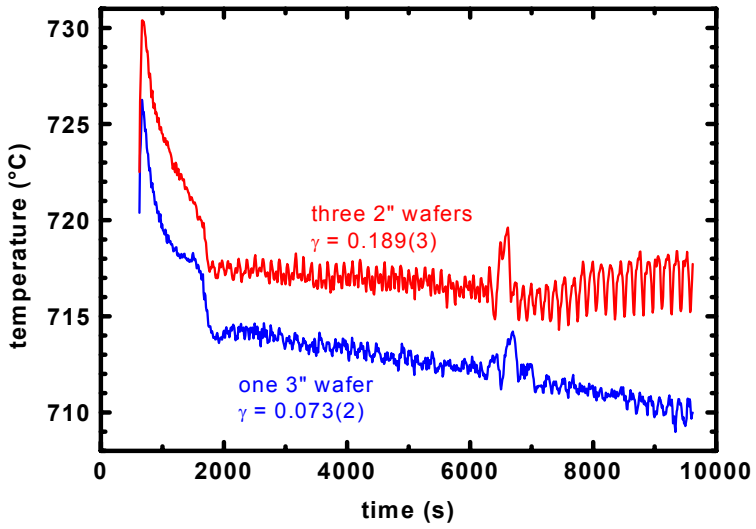

Fig 5.1: Comparison of reflectance-corrected pyrometry on single and multiple-wafer systems. Both traces are for 850 nm VCSEL structures with high reflectance values.

Fig. 5.1 compares the results of γ-corrected pyrometry on identical device structures. The top trace is the temperature extracted from a wafer carrier holding three 2" wafers. The pyrometer viewed part of the wafer carrier as the signal was averaged over many revolutions of the rotating disk. The second trace is the temperature extracted from a single 3" wafer in the same MOCVD machine. In this case, the pyrometer always viewed just the wafer. Although there are some artifacts on the second mirror of the 3-wafer run, it appears that Eq. [4.3] is successful in determining the wafer temperature. As expected, the multiple-wafer system requires a larger γ factor to account for the increase in uncompensated thermal emission from the wafer carrier.

The optimum viewing location for a multiple-wafer pyrometer would be at the disk radius in which the wafers are nearly touching. This minimizes the amount of background thermal radiation viewed by the pyrometer.

6 Summary

The surface temperature of a semiconductor wafer can change during thin film growth. The thin films alter the total hemispherical emissivity which affects the radiative heat transfer that controls the wafer temperature. Thin film deposition also affects the emissivity at the single wavelength used to measure temperature with pyrometry, causing large temperature measurement errors.

With care, it is possible to extract artifact-free wafer surface temperatures using reflectance-correcting pyrometry. Although the absolute accuracy of the method has not been firmly established, consistent behavior has been demonstrated that allows one to use pyrometric temperatures to set MOCVD growth conditions. The following must be established to ensure success in a reflectance-correcting pyrometer measurement (The section in the report relevant to each of these topics is provided in parentheses):

The temperature is extracted from two signals: 1) the thermal emission, s, from the hot wafer surface, and 2) the specular reflectance, R, of the wafer. These measurements must be performed with the following constraints:

1. The substrate must be flat, smooth, and opaque at the measured wavelength and temperature. (1.5.2).
2. The signals are best collected at normal incidence over a narrow range of angles about the normal, typically 2-3 degrees. It is best if both signals travel over the same optical path. (2.1.1)
3. The signals should be measured over as narrow a wavelength bandpass as is practical. 10 nm is acceptable. (2.1.2) Larger bandwidths cause uncorrectable artifacts.
4. The optics should be arranged to reject stray thermal radiation and tolerate wafer tilt. (E).
5. The instrument may be self-calibrated *in situ* by measuring the two signals, s_{cal} and R_{cal} at a known wafer surface temperature, T_{cal}. (2.2.1).
6. Temperature overcompensation artifacts may be reduced by using a DBR structure to extract a fit to the universal γ correction factor. This factor simultaneously accounts for fixed, systematic errors in reflectance scaling and offset, and fixed systematic contributions from stray wafer carrier thermal emission and wafer thermal emission scaling errors. (4.3 and F).
7. The following equation is used to obtain a temperature (in K) (4.3.1):

$$\frac{1}{T} = \tau - \frac{\lambda}{c_2} \ln \frac{s}{1 - R + \gamma}$$

$$\tau = \frac{1}{T_{cal}} - \frac{\lambda}{c_2} \ln \frac{1 - R_{cal} + \gamma}{s_{cal}}$$

with $c_2 = 1.438769 \times 10^7$ nmK.

6.1 Acknowledgements

W. G. Breiland would like to acknowledge the active collaboration of all participants in this study. In particular, Larry Bruskas provided countless design ideas for the pyrometer and constructed all of Sandia's instruments. Andy Allerman and Terry Hargett put up with considerable inconvenience in installing and testing the pyrometer. They performed all the growth runs presented in the report. Alex Gurrary and Vadim Boguslavskiy of EMCORE corporation gave insightful guidance on many subjects to explore to improve the performance of the pyrometer. Finally, we are all indebted to Prof. Kirchhoff for providing three laws that made this project possible: 1) emissivity/absorptivity equivalence, 2) diffraction theory for rough surface scattering, and 3) electrical circuit analysis for analog/digital filter matching.

7 References

1. D. P. DeWitt and G. D. Nutter, eds. “Theory and Practice of Radiation Thermometry”, John Wiley and Sons, Inc, 1988.
2. R. Siegel and J. R. Howell, “Thermal Radiation Heat Transfer”, Hemisphere Publishing, 1972.
3. P. Drude, “The Theory of Optics”, Dover reproduction of original 1909 text.
4. R. W. Wood, “Physical Optics”, Dover reproduction of original 1934 text.
5. M. Planck, Ann. Physik, 4 (1901) 553.
6. a) W. G. Breiland and G. E. Evans, J. Electrochem. Soc. 138 (1991) 1806; b) G. Evans and R. Greif, J. Heat Transfer, 109 (1987) 928.
7. J. Strong, “Procedures in Experimental Physics”, Prentice-Hall, 1938, p. 376.
8. J. C. Stover, “Optical Scattering: Measurement and Analysis”, SPIE Optical Engineering Press, 1995.
9. E. D. Palik, ed., “Handbook of Optical Constants of Solids”, Academic Press, V I-III (1998).
10. M. A. Afromowitz, Sol. State Comm. 15 (1974) 59.

A. Appendix: Heat and Radiation Transfer in the RDR

Conductive / Convective Heat Transfer

Heat and mass transfer is straightforward to calculate in an ideal rotating disk reactor (RDR). The detailed analysis is outside the scope of this report, but is fully described in references [6a,b]. The important result for surface temperature determinations is that one part of the problem solution yields a dimensionless thermal conductivity times the derivative of a dimensionless temperature at the disk surface. Surprisingly, one obtains virtually the same value (in dimensionless units) for this gradient for <u>all</u> gases and mixtures of gases:

$$\hat{k}\left.\frac{\partial \hat{T}}{\partial \hat{z}}\right|_{\hat{z}=0} \cong -0.29$$

The above dimensionless quantities are defined in terms of the actual gas properties at room temperature (rt):

$$\hat{k} \equiv k / k_{rt}$$

$$\hat{T} \equiv \frac{T - T_{rt}}{T_{wafer} - T_{rt}}$$

$$\hat{z} \equiv z\sqrt{\frac{\omega}{\nu_{rt}}}$$

where k is the gas mixture thermal conductivity in W/cm•K, ω is the disk rotation rate in radians/s, and ν is the gas mixture kinematic viscosity in cm^2/s.

From Fick's law of heat transfer, we have an expression for the one-dimensional heat flux, q, (W/cm^2) leaving the surface of the disk:

$$q = -k\left.\frac{\partial T}{\partial z}\right|_{z=0}$$

From all the above equations, one may derive an expression for the heat flux lost from the surface of a rotating wafer:

$$q_{RDR} = 0.29 k_{rt}\sqrt{\frac{\omega}{\nu_{rt}}}\left(T_{wafer} - T_{rt}\right) = h\left(T_{wafer} - T_{rt}\right),$$

where h is called a "heat transfer coefficient" that describes the collective loss from a combination of conduction and convection. The expression for the heat transfer coefficient applies to all gas mixtures, pressures, and spin rates. A typical value for MOCVD applications, 2% AsH_3 in H_2, 60 torr, 1000 RPM, is h = 1.7 mW/cm^2K.

Radiative Heat Transfer

The only other source of energy loss from the top surface of the wafer is that due to radiation. Assuming that the walls of the MOCVD reactor are near room temperature and that the chamber acts as a large enclosure for the wafer, the radiative heat flux from the wafer surface is given by the Stephan-Boltzmann law [2]:

$$q_{rad} = \varepsilon_{tot}\sigma_{sb}\left(T_{wafer}^4 - T_{rt}^4\right).$$

σ_{sb} is the Stephan-Boltzmann constant, 5.67×10^{-12} W•cm^{-2}•K^{-4}. The above equation is derived from the net exchange of radiation energy between the wafer surface and the walls of the reactor. It is only approximately true. An accurate calculation would require detailed knowledge of the emissivity of all reactor surfaces and the geometrical "view factors" between wafer and reactor wall. In the limit of a large enclosure, the wall emissivity cancels out, yielding the above simple expression [2].

The emissivity term used in heat transfer calculations is the "total hemispherical emissivity", obtained by integrating the emissivity described in sec 1.4.2 over all wavelengths, all incidence angles, and both polarizations:

$$\varepsilon_{tot}(T) = \frac{\pi \sum_{\sigma=s,p} \int_0^{\pi/2} d\theta \int_0^{\infty} d\lambda \quad \varepsilon(\lambda,\theta,\sigma,T) L_b(\lambda,T)\cos\theta\sin\theta}{\sigma_{sb}T^4}.$$

Note that the emissivity integration is weighted by the blackbody radiance. A calculation of ε_{tot} from first principles thus requires the determination of $\varepsilon(\lambda, \theta, \sigma, T)$ for all incidence angles, both polarizations, and all wavelengths for which $L_b(\lambda, T)$ is significantly larger than zero.

Combined Conduction / Convection and Radiative Heat Transfer

Under steady-state conditions, the energy flux from the heater is balanced by the energy flux losses from the surface of the wafer. We can avoid the complicated modeling of the energy flux from the heater by starting with an assumed steady-state temperature and looking at the effects that perturbations in h and ε_{tot} have on the surface temperature.

Assume that some steady-state temperature, T_{ss}, has been attained during the MOCVD run. This temperature is reached for fixed values of h and ε_{tot}, i.e. the gas mixture, pressure, and spin rate of the disk are not altered (constant h), and thin-film deposition is not occurring (constant ε_{tot}). Under these conditions, the heater energy input flux must be equal to the total wafer surface losses:

$$q_{heater} = q_{rad}^{ss} + q_{RDR}^{ss}$$

Now assume that the wafer surface is perturbed either by a change in the heat transfer coefficient or in a change in total emissivity. These changes can take place very quickly compared to the

time that the heater takes to change its energy flux. Assuming, therefore, that the heater flux stays constant, the following relationship is true:

$$q_{heater} = q^{ss}_{heater}$$
$$q_{RDR} + q_{rad} = q^{ss}_{RDR} + q^{ss}_{rad}$$
$$h\left(T_{wafer} - T_{rt}\right) + \varepsilon_{tot}\sigma_{sb}\left(T^4_{wafer} - T^4_{rt}\right) = h_{ss}\left(T^{ss}_{wafer} - T_{rt}\right) + \varepsilon^{ss}_{tot}\sigma_{sb}\left(T^{ss4}_{wafer} - T^4_{rt}\right)$$

This provides a quartic equation for T_{wafer} that may be solved using Newton-Raphson iteration. The starting guess in the iteration is T^{ss}_{wafer}.

Radiation-dominated heat transfer special case

If radiative losses dominate over the conduction/convection losses, and the wafer temperature is significantly above room temperature, the above equation reduces to a simpler expression that can be used for quick estimates of the wafer temperature:

$$T_{wafer} = T^{ss}_{wafer}\left(\frac{\varepsilon^{ss}_{tot}}{\varepsilon_{tot}}\right)^{1/4}.$$

This expression implies the well-known fact that changes in surface temperature are weakly dependent on changes in the total emissivity. The fractional change in temperature is given by the fourth root of the emissivity ratio. A 1% ratio yields only a 0.25% change in temperature. However, at 1000 K a 0.25% change is still 2.5 degrees.

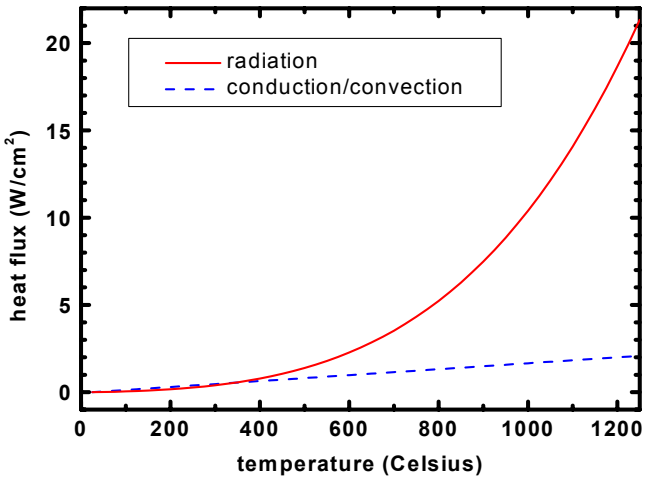

The figure above compares energy fluxes from radiation vs conduction/convection for typical conditions in Sandia's D125 EMCORE reactor (60 torr, 1000 RPM, ~2% AsH_3 in hydrogen). These conditions yield a heat transfer coefficient of h = 1.7 mW/cm^{2}K. Flux contributions are equal at 350 °C, and radiation losses become ten times greater than conductive/convective losses at 1250 °C.

B. Appendix: Surface Roughness Measurements

If the surface of a wafer becomes rough, light from a reflectance experiment will no longer scatter in a narrow beam with specular reflectance. A drop in the measured reflectance will lead to temperature overcompensation effects because it will manifest itself as a reflectance scaling error. (see 3.4). Surface roughness measurements were therefore made on wafers whose reflectance-correcting pyrometry temperatures exhibited overcompensation effects to determine whether roughness could be responsible. Four wafers with films grown by EMCORE were examined as well as a bare substrate wafer for reference.

Roughness measurements were made with Atomic Force Microscopy (AFM) and a light scattering technique called Total Integrated Scatter (TIS) [8]. AFM measurements are quite accurate, but they do not cover a large area such as would be used in a typical reflectance-correcting pyrometry experiment. According to Stover [8] there is no single RMS height number that characterizes the roughness of a surface. As larger and larger areas are probed with a surface roughness tool, more widely-spaced surface features are sampled. This generally results in the RMS height distribution increasing with increasing sampled area. The optical TIS technique was therefore used to confirm that the surface roughness appropriate to the loss of reflectance was measured.

AFM Results

AFM measurements yielded RMS surface roughness heights between 6 and 9 Å over a 10 μm × 10 μm area. Diffraction theory for light scattering predicts that the specular reflectance is attenuated according to the following relationship[8]:

$$\frac{R}{R_0} = \exp\left[-\left(4\pi\sigma / \lambda\right)^2\right]$$

where R_0 is the reflectance of a perfectly smooth surface, σ is the RMS roughness, and λ is the wavelength of light. From the above formula, one would predict that reflectance attenuation values would range from 0.99993 to 0.99984 for RMS roughness from 6 to 9 Å, respectively. This result predicts that surface roughening has a completely negligible effect on pyrometry.

TIS Results

The figure below shows a schematic of the TIS apparatus. An integrating sphere with a small hole in the bottom is placed over the wafer. A HeNe laser beam illuminates the wafer through a small hole in the top of the integrating sphere. The wafer is manipulated to retro-reflect the laser beam out the top hole. A light-baffled detector is placed in the side of the integrating sphere to measure the light that is scattered into 2π sr. A second detector is placed outside the integrating sphere to measure the specular reflectance of the wafer. Calibration of the system is done with a 99.9% mirror and a spectralon diffuse scattering surface. TIS is defined to be the fraction of light scattered in all but the specular direction. It is 0 for a perfectly smooth ($\sigma = 0$) surface and 1 for a very rough ($\sigma >> \lambda$) surface.

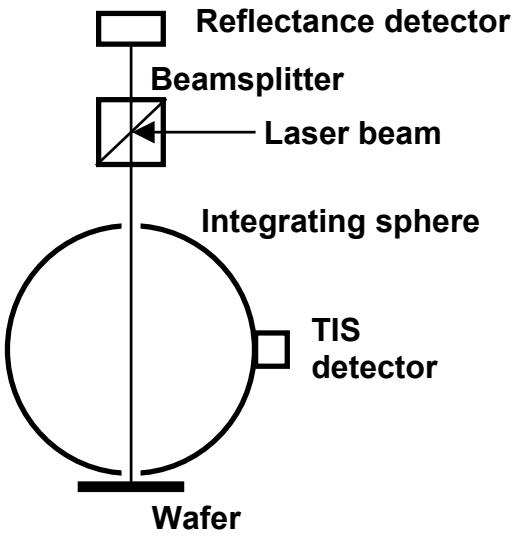

Very little scattering could be detected from any of the wafer samples, including the bare substrate wafer. In fact, the dielectric mirror used to calibrate the specular reflectance scattered more light than any of the samples. The scattering was so small that much of the TIS signal was most likely due to stray light from the laser beam scattering off the upper aperture. Even with this systematic error, TIS values were well below anything that could be considered significant. Given that the scattering would be a factor of $\exp(900^2 / 633^2) = 7.5$ times less for 900 nm light, we may conclude that scattering from rough surfaces is definitely not responsible for the temperature overcompensation effect. The table below summarizes the results for the roughness experiments. The column labeled "R/R_0 TIS @900 nm" lists the expected attenuation factors from scattering losses for the reflectance-correcting pyrometry. In all cases, the effect is negligible.

sample	σ (Å) AFM	R/R_0 AFM (predicted)	TIS	R/R_0 TIS @ 900 nm	R/R_0 TIS @ 633 nm
bare	8.9	0.999846	0.0021	0.999720	0.9979
6m132	7.3	0.999896	0.0029	0.999613	0.9971
6m166DH	6.4	0.999920	0.0019	0.999747	0.9981
6m179	8.0	0.999875	0.0018	0.999760	0.9982
6m214BR	8.9	0.999846	0.0025	0.999667	0.9975

C. Appendix: Effect of a Semitransparent Film on Thermal Radiation

We proceed to obtain an expression for the thermal emission from the situation pictured in Fig. 3.1 and reproduced for convenience, below

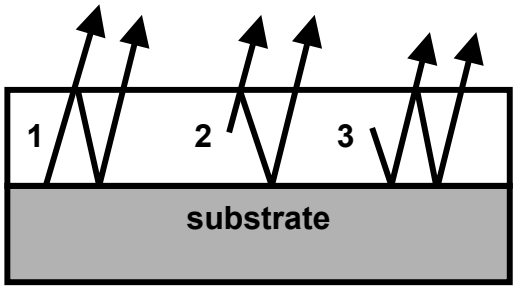

First, we must consider how to deal with thermal radiation generated within the bulk of a material that propagates to the surface. Start with a flat slab of material with absorption coefficient, α. When heated, this material generates thermal radiation that will propagate out from the bulk to the surface over the penetration depth of the material. We need only consider radiation that propagates in the normal direction. The thermal radiation may then be described as a plane-wave source term, $J(T)$ (units of radiance cm^{-1}), which is a constant value everywhere inside the solid. The total flux of energy reaching the surface of the substrate from a depth, *d*, is given by the sum of contributions from each source term at a distance x inside the substrate, attenuated by internal absorption on its way to the surface:

$$\Phi = \int_0^d J \exp(-\alpha x) dx = J(1 - \exp(-\alpha d))/\alpha$$

If the material is either a) strongly absorbing, $\alpha >> 1$, or b) very thick $d \to \infty$, we have an opaque substrate, and the thermal flux reaching the surface of the substrate is just J/α. Upon crossing the air/substrate interface, this flux will be reduced by an internal reflection loss factor $1 - R$, where *R* is the substrate reflectance. Comparing this quantity with the Kirchhoff's law expression, we note

$$(1 - R)J/\alpha = (1 - R)L_b$$

which relates the volume thermal plane-wave source term to the blackbody radiance.

$$J/\alpha = L_b$$

Now consider the effects of internal reflections. A semi-transparent film, thickness *d*, is deposited on an opaque substrate. Reflectance can occur at the air/film substrate *R*, and at the film/substrate interface, R_s.

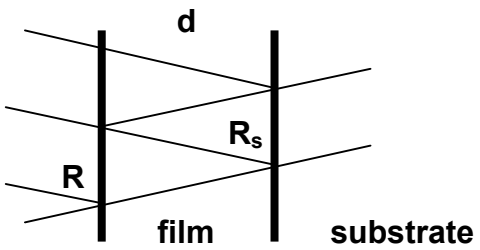

The total external reflectance R_{tot} from this structure is obtained by summing up all fluxes that occur from multiple internal reflections. For simplicity, we shall ignore thin-film interference effects, but still account for all internal reflections. The semitransparent film attenuates the flux by τ for every pass through the film thickness, d: $\tau = \exp(-\alpha d)$. We construct a geometric series describing the multiple reflections and obtain an expression for the total external specular reflectance:

$$R_{tot} = R + (1-R)\tau R_s \tau (1-R)\left(1 + RR_s\tau^2 + \left[RR_s\tau^2\right]^2 + \ldots\right) = R + \frac{(1-R)^2 R_s \tau^2}{1 - RR_s\tau^2}$$

Now consider a detailed accounting of all the thermal radiation contributions to the total thermal emission at the surface, shown in the figure above. These arise from three contributions: 1) Radiation from the substrate. 2) Radiation from the film throughout its thickness, d, directed toward the surface. 3) Radiation from the film throughout its thickness, d, directed toward the substrate and reflected off the film/substrate interface back to the surface. Mathematically we have:

$$L_1 = L_b(1-R_s)\tau(1-R)\left(1 + RR_s\tau^2 + \left[RR_s\tau^2\right]^2 + \ldots\right)$$
$$L_2 = L_b(1-R)(1-\tau)\left(1 + RR_s\tau^2 + \left[RR_s\tau^2\right]^2 + \ldots\right)$$
$$L_3 = L_b(1-\tau)R_s\tau(1-R)\left(1 + RR_s\tau^2 + \left[RR_s\tau^2\right]^2 + \ldots\right)$$

The source term for L_1 is the blackbody radiance times the emissivity of the substrate, $L_b(1 - R_s)$. The source term for L_2 and L_3 is

$$\Phi = J\left(1 - \exp(-\alpha d)\right)/\alpha = L_b(1-\tau)$$

Summing these three contributions, we obtain

$$L_{tot} = L_1 + L_2 + L_3 = L_b \frac{(1-R)\left(1 - R_s\tau^2\right)}{1 - RR_s\tau^2}$$

Expanding the numerator and recollecting terms reveals that this expression is just the expected Kirchhoff's law result:

$$L_{tot} = L_b\left(1 - R_{tot}\right)$$

The conclusion is that Kirchhoff's law, which is based on global energy conservation and second law arguments, will always predict the outcome of any detailed thermal radiation treatment, no matter how complex the film structure. Provided that the substrate is flat and opaque, the observed thermal emission from an arbitrarily complex multiple-layer film structure must be given by the above simple Kirchhoff's law result.

D. Appendix: Matching Analog and Digital Filters

Analog RC Network

The simple RC network is frequently used as a low-pass filter for DC signals. It is characterized with a time constant, τ, given by $\tau = RC$, where R is the resistance in ohms and C is the capacitance in Farads. A step-input signal sent through this filter will completely settle to its input value after five time constants. The frequency response of the filter is flat (zero slope) at 0 Hz and has a cutoff at $2\pi f_c = 1 / \tau$, where f_c is the cutoff frequency in Hz. Signals at the cutoff frequency are attenuated by "3 dB" (dB = -20 $\log_{10}$ (V_{out} / V_{in})), which is a factor of 1 / $\sqrt{2}$ = 0.7071. Beyond the cutoff frequency, signals are attenuated at a rate of 6 dB per octave (a factor of 2 for every doubling of the frequency), or, equivalently, the signal is attenuated a factor of 10 for every frequency decade. This attenuation rate is called the "frequency rolloff" of the filter.

For filtering of DC signals, the 6 dB per octave rolloff rate is not as strong as one would like for stable signal sources. The rolloff rate may be increased to 24 dB/octave (10^4 attenuation per decade) simply by cascading four RC stages together as shown in the figure below.

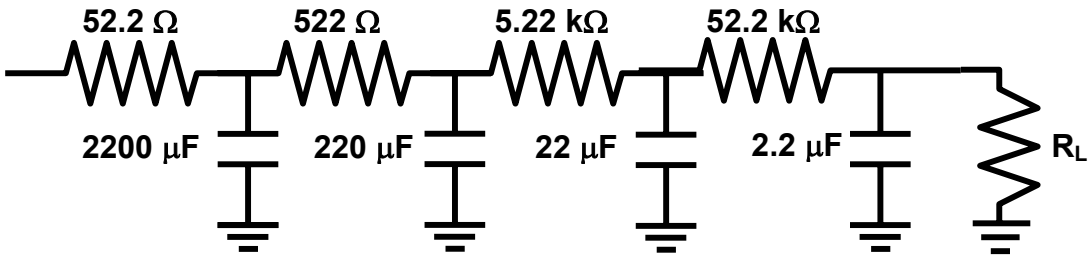

Each stage in this filter has a time constant of 0.115 s. If this network is connected to a high impedance load of R_L > 1 MΩ, it will have an aggregate time constant of 0.3 s, a cutoff frequency of 0.531 Hz, and a rolloff of 24 dB/octave. The figure below shows a plot of the frequency response. Also shown is the response of a single-stage filter.

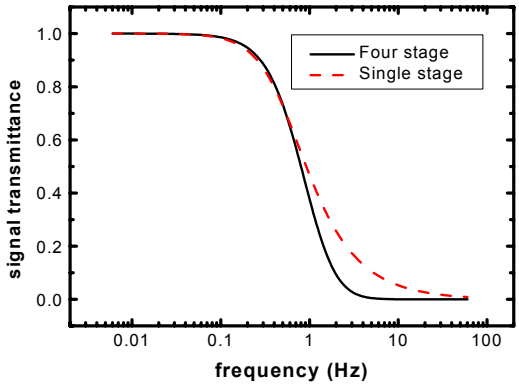

Note the superior noise suppression of the four-stage filter at 10× the cutoff frequency. At 5.3 Hz the single-stage filter passes 10%, but the four-stage passes only 10^{-4}.

The choice of component values is determined by the nature of RC networks. In order to minimize coupling between stages, the resistance values are chosen to be a factor of ten different for each stage while maintaining the same time constant, *RC*. This passive network is effective only when the output impedance of the signal source is low and the load resistance, R_L, is high. If these conditions can be met, the four-stage filter provides a very simple sharp cutoff filter with low attenuation and trouble-free operation.

The Butterworth Digital Filter

The time and frequency response of the single-stage RC filter can be emulated exactly with a Butterworth digital filter. Given a stream of data in an array, y[], the smoothed output of the Butterworth filter, y_s[], is given by the very simple formula:

$$y_s[i] = a\big(y[i] + y[i-1]\big) + by_s[i-1]$$

The two coefficients, a and b, are determined by the time constant, τ, and the time interval between data points, Δ:

$$a = \frac{1}{1+c}; \quad b = -\frac{1-c}{1+c}; \quad c = \frac{1}{\tan(\Delta/2\tau)}.$$

The Butterworth filter is known as a *recursive* filter because the smoothed value depends not only on the present and prior values of the raw data stream, but the prior value of the smoothed stream as well.

A four-stage Butterworth filter is easy to construct by using the output stream from one Butterworth stage as input to the next stage. The resulting filter emulates a four-stage analog RC filter with the following important differences: **1)** The time constant for the four-stage Butterworth filter is lengthened by a factor of $1/\sqrt{2^{1/4}-1}$. Thus, if one wants a four-stage Butterworth filter with a time constant, τ_4, then one must use $\tau = \tau_4\sqrt{2^{1/4}-1}$ as the time constant in each stage. **2)** The Butterworth emulates an ideal four-stage analog RC filter that has no interactions between stages. In order to match a real analog RC filter (which has inter-stage interactions) to the performance of a four-stage Butterworth, one must perform a Kirchhoff analysis of the network to determine the values of R and C for each stage.

Matching Analog and Butterworth Four-stage Filters

It is possible to build an analog filter that has exactly the same response as a four-stage Butterworth filter. Typically one chooses four capacitors that have nominal values differing by ×10, as illustrated in the network above. The capacitance for each component, C_i, i = 1,4 is then accurately measured. For a given load resistance, R_L, and desired time constant, τ, one must then choose precision resistors, R_i, i = 1,4 that will provide the same time and frequency response as a four-stage Butterworth filter with time constant, τ. This is accomplished by solving a rather complicated algebra problem. Using Kirchhoff's law for electrical networks, the relationship between the input and output voltages is given by a matrix equation:

$$\begin{bmatrix} V_L \\ V_L / R_L \end{bmatrix} = M_1 M_2 M_3 M_4 \begin{bmatrix} V_{in} \\ i_{in} \end{bmatrix}$$

with

$$M_n = \begin{bmatrix} 1 & -x\tau / C_n \\ -j\omega C_n & 1 + j\omega x\tau \end{bmatrix}$$

V_L is the voltage at the load, R_L. V_{in} is the input voltage, and i_{in} is the input current. The time constant for each stage is expressed as a yet to be determined factor, x, times the desired time constant, τ. ω is the circular frequency and j is $\sqrt{-1}$. Each stage is constrained to have the same time constant, $x\tau$, and the values of the resistances must be chosen such that each stage has the same RC value:

$$R_1 C_1 = R_2 C_2 = R_3 C_3 = R_4 C_4 = x\tau$$

The matrix equation yields two simultaneous equations that can be used to eliminate the unknown current, i_{in} and obtain a single equation for V_{in}/V_L as a function of x and ω:

$$\frac{V_{in}}{V_L} = 1 + ax + (bx + c)\varpi + (dx + e)\varpi^2 + (fx + g)\varpi^3 + \varpi^4; \quad \varpi = j\omega x\tau$$

with

$$a = \frac{\tau}{R_L}\left(1/C_1 + 1/C_2 + 1/C_3 + 1/C_4\right)$$

$$b = \frac{\tau}{R_L}\left(1/C_2 + C_2/C_1C_3 + 2/C_3 + C_3/C_1C_4 + C_3/C_2C_4 + C_2/C_1C_4 + 3/C_4\right)$$

$$c = C_4/C_1 + C_4/C_2 + C_4/C_3 + C_3/C_1 + C_3/C_2 + C_2/C_1 + 4$$

$$d = \frac{\tau}{R_L}\left(1/C_3 + C_3/C_2C_4 + C_2/C_1C_4 + 3/C_4\right)$$

$$e = C_4/C_2 + C_2C_4/C_1C_3 + 2C_4/C_3 + C_3/C_1 + 2C_3/C_2 + 2C_2/C_1 + 6$$

$$f = \frac{\tau}{R_L C_4}$$

$$g = C_4/C_3 + C_3/C_2 + C_2/C_1 + 4$$

V_{in} may be eliminated by noting that at $\varpi = \omega = 0$ we have

$$\frac{V_{in}}{V_L(x, \varpi = 0)} = 1 + ax$$

Dividing through by $1+ax$ will eliminate V_{in}. We may eliminate the variable ω from this equation by matching the 3 dB point in the attenuation curve to that of the Butterworth filter. First, note that at the 3 dB point we have the two conditions:

$$\left|\frac{V_L(x,\varpi=0)}{V_L(x,\varpi=jx)}\right|^2 = 2 \quad and \quad \omega\tau = 1$$

Substituting these expressions into the above polynomial yields, after considerable algebra, an eighth-order polynomial in the single variable x:

$$-1-2ax+\left(c^2-a^2-2e\right)x^2+2(bc-ae-d)x^3+\left(2-2ad+e^2+b^2-2cg\right)x^4+$$
$$2(a+be-bg-cf)x^5+\left(d^2-2e+g^2-2bf\right)x^6+2(fg-d)x^7+\left(1+f^2\right)x^8=0$$

This polynomial is easily solved for x using Newton-Raphson iteration with the uncoupled value $x=\sqrt{2^{1/4}-1}=0.435$ as a starting guess. Once x is found, the resistance values are obtained with

$$R_1C_1 = R_2C_2 = R_3C_3 = R_4C_4 = x\tau$$

Precision resistors are available in a wide variety of values, unlike capacitors. Thus, it is not difficult to find resistors that closely match the R_i values obtained from the above equation. The attenuation of the passive filter is obtained from

$$\frac{V_L(x,\varpi=0)}{V_{in}} = \frac{1}{1+ax}$$

For the high load impedance typically found in D/A converters and other instrumental amplifiers, the attenuation is negligible.

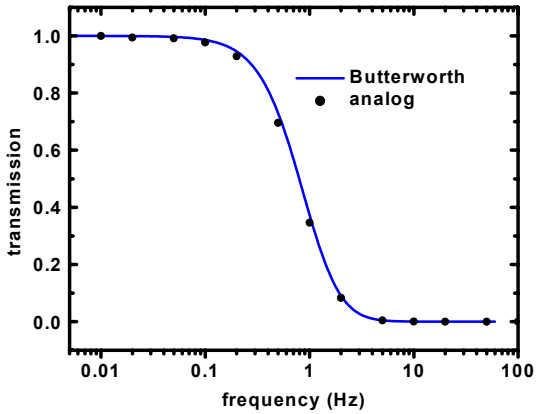

The figure above shows the measured (points) and theoretical (line) response of a four-stage analog (points) and a Butterworth (line) filter. Measured capacitance values for the analog filter were 2200, 233, 26, and 2.18 μF. Resistance values calculated with the above formulas were 52.4, 497, 4.54k, and 52.2k ohms. The attenuation of the network is only 0.994 going into a load resistance of 10 MΩ.

As seen in the above figure, experiments verify that the above matching scheme allows one to build a four-stage analog filter whose measured frequency response very closely matches the frequency response of a four-stage Butterworth digital filter. Such matching is critical if a filtered analog signal is divided by a value obtained by digital filtering from another signal source. An exact match will ensure that the time response and phase shifts inherent in the two filters are the same. This maintains the fidelity of the ratio.

E. Appendix: Optics of Stray Thermal Emission Sources

Stray light from surfaces other than the wafer can be minimized using standard imaging methods. For pyrometry applications, it is best to image the end of the receiving fiber on the wafer as illustrated in the figure below. This arrangement has several benefits. First, the beam of light used for reflectance measurements is guided into the receiving fiber, independent of the wafer tilt. This happens because the laws of optics ensure that any ray launched from the surface of the wafer will be imaged to its conjugate point on the receive fiber, provided that 1) the beam is launched from within the spot defined by the image of the receive fiber on the wafer, and 2) the lens manages to capture the emerging beam of light.

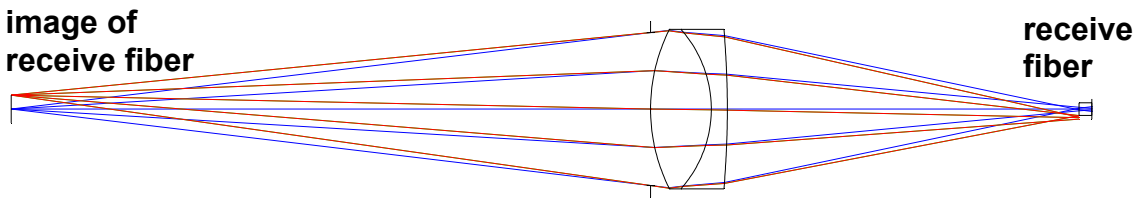

Second, the imaging process acts as a "spatial filter". Any light launched from the wafer surface that does not start within the image spot of the receive fiber will not be directed into the receiving fiber aperture. In the figure above, rays starting at the far left above the receive fiber image spot are seen to just miss the aperture of the lower part of the receive fiber. This spatial filtering action rejects all rays that do not simultaneously pass through the fiber image spot on the wafer and the receiving lens. Third, stray radiation that starts from a source that is not in the focal plane (i.e. at the wafer) will be out of focus at the receive fiber, even if some rays manage to pass through the image and the lens. As a result, only a fraction of the rays that start from such a source actually manage to get into the receive fiber. This fraction drops off rapidly as the source is displaced farther from the focal plane (wafer surface). Fourth, imaging produces a well-defined spot on the wafer from which temperature and reflectance is measured. The focal length of the lens may be chosen to define a desired magnification and spot-size on the wafer.

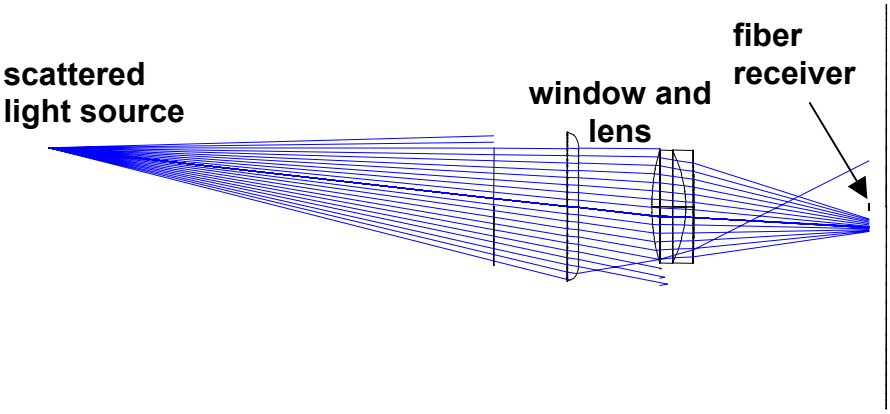

Unfortunately, spatial filtering is not the only issue in stray light effects. The figure above shows a detailed ray tracing of light starting from a point on the wall of a tube (at far left of figure), passing through an aperture and window with curved surfaces at the edge, hitting a lens, and then

reaching the plane that contains the receiving fiber for the pyrometer. (The beamsplitter is not included in this figure for clarity). In this case, spatial filtering is very effective at ensuring that the spot of light at the fiber plane is out of focus and is displaced such that virtually no light can reach the fiber aperture. However, the curvature on the window has acted as a lens for one extreme ray. It is therefore possible that a small fraction of light can reach the fiber via this strong deviation.

There is another possible source of stray light from sources located outside the spatial filter limits. In the above figure, note that a large number of rays from the scattering site hit the window, the receive lens and the beamsplitter. Dust and imperfections in the optics, coatings and probe walls can scatter this light in all directions. Although the fractional scattering may be very small, if enough sources of scattered light with high radiance reach the receiving optical fiber, it is possible that a significant background signal can be recorded. This background will become most noticeable, and will produce the largest errors, when the thermal emission from the wafer drops to low values (high *R*).

Zeta Scattering Sources

Thermal emission from the wafer carrier that undergoes at least one bounce from a wafer surface before adding to the stray-light signal is described by the ζ factor.

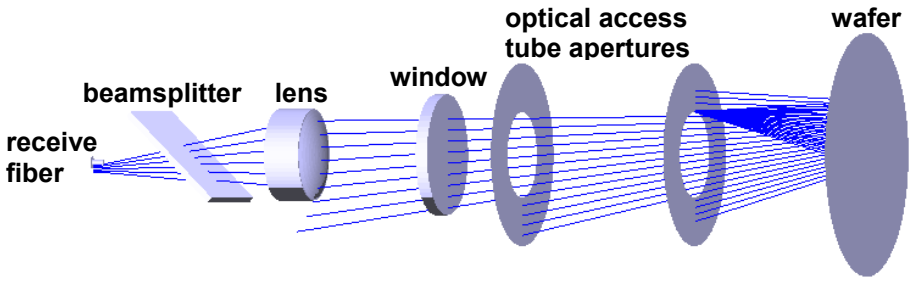

The figure above illustrates schematically how stray radiation scattered off the inlet near the optical access tube bounces off the wafer, enters the optical access tube and is partially accepted by the receive fiber aperture. The figure shows only a single fan of rays from a single point source on the bottom of the reactor inlet. The ζ scattering represents the sum of all such possible point sources that can direct some light into the receive optical fiber.

Using a ray tracing program for the geometry of Sandia's EMCORE reactor, it was not possible to capture any ζ factor rays from the inlet. Spatial filtering was very effective at excluding stray light from a perfectly aligned system. However, gross tilts (0.5° in the x and y direction) of the wafer did allow a very small fraction of light from the inlet to be accepted by the receive fiber aperture.

Different geometries can provide a significant out-of-focus virtual source of stray ζ light. A detailed ray-trace analysis may be useful in suggesting alternative light collection schemes that will reject the out-of-focus reflected inlet virtual source. Wafer tilt must be considered in such an analysis.

F. Appendix: Determination of the Gamma Factor

This appendix presents detailed derivations for the empirical determination of γ. Two different methods are presented that yield essentially the same degree of overcompensation correction.

Assume that one has a set of data consisting of the thermal emission signal, *s*, and the reflectance, *R*, taken during the growth of a structure that yields large variations in *R*. We wish to extract a value for the constant, γ, that will minimize temperature overcompensation artifacts. If the surface temperature of the wafer stays relatively constant while the structure is grown, we may use either of the two methods to find the value of γ.

Linear Fit Method

From Eq. [4.2] we have, at constant temperature, a simple linear relationship between *s* and *R*:

$$s = C(1+\gamma) - CR$$

The slope and intercept of a linear fit to *s*(*R*) may be used to eliminate the unknown constant, C, and determine the value for γ:

$$s = A - BR$$

$$\gamma = \frac{A}{B} - 1$$

Although one must maintain a constant temperature over the segment of data used to determine γ, the actual value of the temperature does not have to be known because it is implicitly contained in the common factor, C.

Minimum variance method

From Eq. [4.3] we have the expression for calculating a temperature from a given *s* and *R*:

$$\frac{1}{T} = \tau - \frac{\lambda}{c_2} \ln \frac{s}{1 - R + \gamma}.$$

The ratio given in the ln() function leads to artifacts unless γ is adjusted to minimize them. The minimum variance method argues that the ratio in the ln() term will deviate the least from its mean for an optimal choice of γ. If the temperature is constant, then the ratio is also constant. However, a direct minimization of the variance can also accommodate slow drifts in temperature as the structure is grown. As with the linear fit method, the actual value of the temperature does not have to be known.

To apply the method, we find the value of γ that minimizes the variance, *V*, of the merit function, $m(\gamma)$:

$$m(\gamma) = \frac{1 - R + \gamma}{s}$$

$$V = \frac{1}{N-1}\sum_{i}^{N}\left(m_i - \overline{m}\right)^2$$

$$\overline{m} = \frac{1}{N}\sum_{i}^{N} m_i$$

(The inverted choice for m avoids a divide-by-zero error should a value for γ be chosen that causes the numerator to be zero.) The sums run over the number of data points, N. The minimum of V is obtained from:

$$\left.\frac{\partial V}{\partial \gamma}\right|_{\gamma_{opt}} = 0$$

Substituting for m in V, taking the derivative, and solving for optimum γ_{opt} yields:

$$\gamma_{opt} = \frac{-\sum_{i}^{N}\left(\frac{1-R_i}{s_i} - \widetilde{R}\right)\left(\frac{1}{s_i} - \hat{s}\right)}{\sum_{i}^{N}\left(\frac{1}{s_i} - \hat{s}\right)^2}$$

$$\widetilde{R} = \frac{1}{N}\sum_{i}^{N}\frac{1-R_i}{s_i}$$

$$\hat{s} = \frac{1}{N}\sum_{i}^{N}\frac{1}{s_i}$$

Error estimate for gamma

It is worth calculating an estimate of the uncertainty in γ_{opt}. This is particularly valuable if a DBR structure is not available for γ determination and the range in reflectance values may be insufficient to extract a meaningful γ_{opt}. A quick visual check for the viability of the gamma determination is obtained from a plot of s as a function of R. If the data show a well-defined straight line, then γ is probably meaningful.

If the temperature is truly constant over the range of data used, then a noise-free merit function would yield exactly the same value for all R_i and s_i at the optimized value of $\gamma = \gamma_{\text{opt}}$. Solving the merit function expression for γ_i at each R_i and s_i pair gives a distribution of γ_i's whose standard deviation, σ, is a measure of the trustworthiness of γ_{opt} as a meaningful value:

$$\gamma_i = s_i\overline{m}(\gamma_{opt}) - 1 + R_i$$

$$\langle\gamma_i\rangle \cong \gamma_{opt}$$

$$\sigma(\gamma_i) << \gamma_{opt}$$

The last equation states that if the standard deviation for the γ_i's is not significantly smaller than γ_{opt}, then the data does not have enough reflectance range to provide a meaningful γ factor. In other words, there are many γ factors that give roughly the same V, so it is impossible to conclude that the use of γ is improving the temperature waveform by reducing artifacts.

Problems With the Determination of Zeta

Adding ζ to the emissivity correcting expressions would appear at first to be straightforward. However, the linear fit method for γ exposes an indeterminacy problem. Using the assumption of a constant temperature, we have, with the addition of a ζR factor to the thermal radiation offset:

$$s = C\left[(1+\gamma) - (1-\zeta)R\right]$$

The expression is still linear, but the fit to slope and intercept values A and B can no longer be used to determine unique values for γ and ζ. Eliminating C yields the following relationship:

$$\frac{A}{B} = \frac{1+\gamma}{1-\zeta}$$

or

$$\gamma = \frac{(1-\zeta)A - B}{B}$$

As a result, there are an infinite number of γ, ζ pairs that satisfy the above linear relationship.

A minimum-variance approach may be formulated to simultaneously optimize for γ and ζ. However, the algorithm is unstable. Examination of the 2-dimensional variance surface as a function of γ and ζ reveals an equal-minimum trough for pairs of γ and ζ satisfying the above relationship. Obviously, the linear expression states the obvious fact that we have three unknown parameters and two known values. No alternative mathematical trick will solve this dilemma with the existing information. A third relationship is needed.

The linear-fit and minimum-variance methods cannot determine a value for ζ because it has been effectively lumped into the overall scaling factor, C, which is also a function of the "true" temperature. Thus, neither method is capable of determining a meaningful value of ζ unless the actual true temperature is known. It is theoretically possible to obtain accurate temperatures using *in situ* calibration once γ has been determined, because *in situ* calibration eliminates the unknown factor, F, in Eq. [4.2].

G. Appendix: Total Emissivity and Temperature During DBR Growth

For the analysis of Appendix F to be valid, the surface temperature of the wafer must not change significantly during the growth of the structure used to extract the thermal emission offsets. Because the radiation lost from the surface depends on the total hemispherical emissivity, thin film deposition can upset the steady-state surface temperature established from the balance between radiative losses and heater-supplied gains (see Appendix A). Because the energy flow into the wafer is roughly constant and radiative transfer is very fast, the surface temperature changes predicted by the quartic formula in Appendix A will instantly track the changes in total hemispherical emissivity. However, if there is significant change in the surface temperature from the above radiative effects, this will ultimately affect the thermal conduction/convection heat transfer characteristics of the entire wafer holder. The altered heat transfer will eventually affect the temperature gradients near the heater thermocouple and the controller will attempt to compensate. This process takes place over minutes, characteristic of the thermal mass of the wafer carrier. It is therefore useful to find a test structure that does not significantly alter the average surface temperature during growth, yet provides large changes in the 900 nm reflectance. A good candidate is a 900 nm DBR mirror structure. This provides wide swings in reflectance at 900 nm, yet produces only a narrow spike in the full reflectance spectrum without significantly changing emissivity in the infrared region where thermal emission is largest. This appendix estimates temperature changes that would be expected to occur during the growth of a 900 nm DBR structure and the effect of these temperature changes on the determination of the γ factor.

Total Emissivity During 900 nm DBR Growth

The change in surface temperature during thin film growth may be estimated by first calculating $R(\lambda, \theta, \sigma, t)$ over a wide range of wavelengths, incidence angles from 0 to 90°, and both *s* and *p* polarizations. The total hemispherical emissivity is then calculated from the expression in Appendix A for ε_{tot} using the special-case relationship, $\varepsilon = 1 - R$ (Eq. [1.13]). Finally, the temperature is obtained by solving the quartic equation in Appendix A.

The expression for the total hemispherical emissivity requires that one integrate over all wavelengths for which the blackbody curve is significantly greater than zero. We choose 1000 K as a representative deposition temperature. At this temperature, *R* must be integrated from 500 nm to 20,000 nm to capture the full blackbody curve. Unfortunately, high-temperature optical constants necessary for calculating the reflectance are not available for such a wide range of wavelengths. We therefore use the data from room temperature measurements as a surrogate for the high temperature data. High temperature causes the optical constant curves to shift to longer wavelengths and broaden, but no other major changes occur. To approximately account for these shifts, we choose to model two different DBR structures made from materials with widely different bandgaps. The first is a mirror constructed from GaAs and 20% AlGaAs layers (62.587 nm GaAs | 65.722 nm $Al_{0.2}Ga_{0.8}As$). The second is a mirror constructed from AlAs and 20% AlGaAs layers (75.72 nm AlAs | 65.722 nm $Al_{0.2}Ga_{0.8}As$).

Room-temperature optical constants for all the above materials over the wavelength range 500 nm to 1000 nm are readily available [9]. The below-bandgap real refractive index values may then be extended to 20,000 nm using the Afromowitz model [10] for AlGaAs.

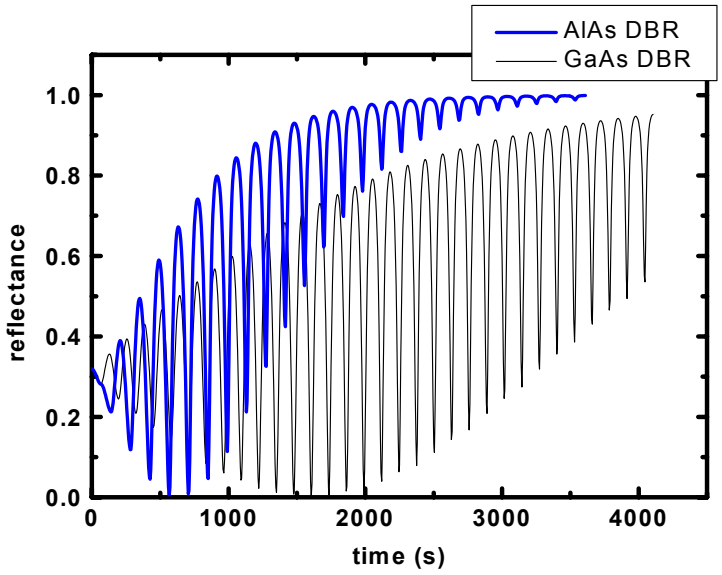

The figure above shows the normal-incidence 900 nm reflectance waveform predicted for 25 stacks of the AlAs|20%AlGaAs DBR and 32 stacks of the GaAs|20%AlGaAs DBR structure. Note that these two waveforms are similar to the shape actually observed for the high-temperature reflectance of the 860 OP-VCSEL structure shown in Fig. 4.1 of section 4.1. The AlAs DBR reaches a high reflectance limit and the low-reflectance values diminish quickly. The GaAs DBR is closer to the observed OP-VCSEL behavior, but takes longer to reach a high reflectance limit. The two calculated waveforms thus roughly bracket some of the features seen

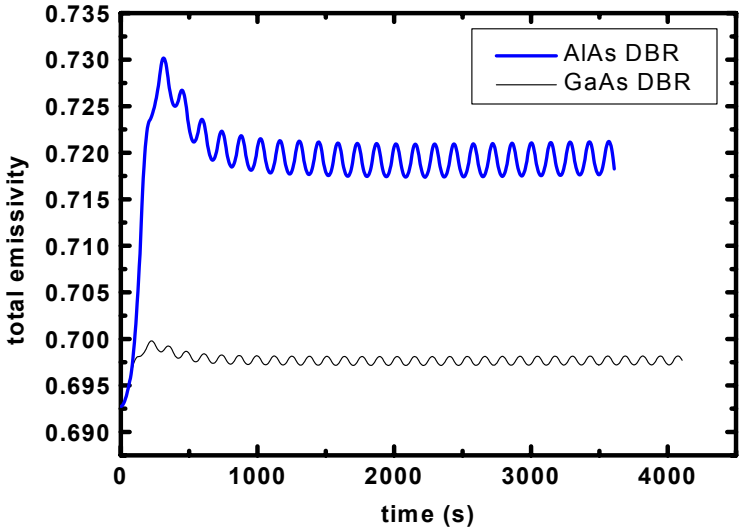

in the experimental waveform.

The figure above shows the total hemispherical emissivity, as given by the expression for ε_{tot}, calculated from the reflectance waveform for each DBR structure, integrated over wavelength,

incidence angle, and polarization. Note that the emissivity still retains features caused by the switching of materials in the quarter-wave stacks. However, the magnitude of the variation is considerably reduced from the single-wavelength reflectance waveform. The largest change in total emissivity during the initial transient in the AlAs DBR is only 6% and spans 0.04 reflectance units. Variations after the initial transient are considerably smaller, less than 0.6% and 0.004 reflectance units.

Wafer Surface Temperature

The figure below shows the temperatures extracted from the quartic formula in Appendix A, using a conduction/convection heat transfer coefficient of 1.7 mW/cm^{2}K. (Ignoring conduction/convection and using the fourth-root approximate formula shifts the curves down by about one degree). As would be expected from its larger changes in emissivity, the AlAs DBR structure is predicted to exhibit larger surface temperature changes. After an initial transient, the AlAs structure is seen to stabilize at a constant average temperature, but retains periodic oscillations with a peak-to-peak amplitude of 1°. The GaAs structure is predicted to stabilize with less than 0.3° peak-to-peak oscillations. Note that both structures drop in temperature from the initial bare-wafer value. This is consistent with higher average total emissivities causing higher potential radiative losses that must be compensated with a drop in surface temperature to

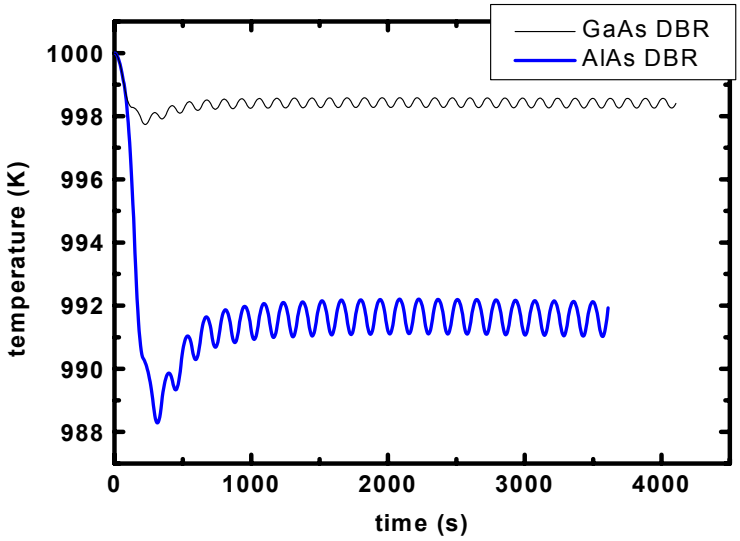

maintain the assumed constant energy flow.

It is important to note that the period of the temperature oscillations seen in the above figure is given by the rate at which the quarter-wave stacks are grown and is not a simple interference oscillation, which would be wavelength dependent. However, the temperature oscillations are seen to track the periodic nature of the 900 nm reflectance interference waveform, and could therefore be confused with an overcompensation effect.

The above figure implies that one should wait for the initial temperature transient to die out before determining the thermal emission offset. This occurs at ~1000 s into the DBR growth after five or six stacks have been grown.

Spectral Behavior

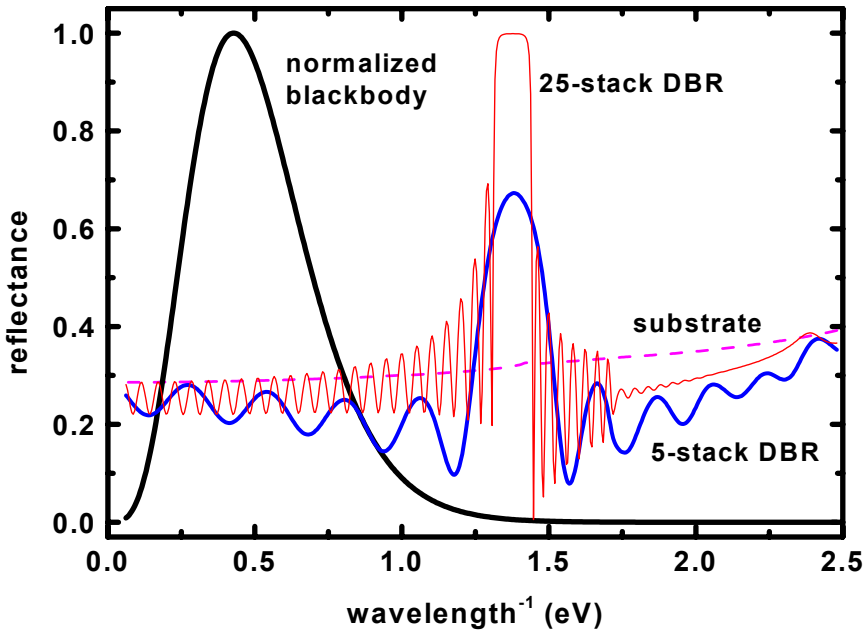

Insight into the emissivity and temperature behavior of the DBR stack may be gained by examining the normal incidence reflectance spectrum during several stages of the DBR growth. The figure above shows three reflectance spectra for the AlAs DBR at the following stages: 1) bare substrate before growth 2) after 5 stacks have been deposited, and 3) the full 25-stack DBR structure. The energy scale is a more convenient way to display the data that ranges from 500 nm to 20,000 nm in wavelength. Also shown is a normalized blackbody spectral radiance curve. From the definition of total hemispherical emissivity, only those spectral features lying within the 0.06 eV (20,000 nm) to 1.25 eV (990 nm) region of the blackbody spectrum will contribute significantly to ε_{tot}. The initial transient in the temperature is explained by the significant difference between the substrate and 5-stack spectrum. The blackbody-weighted average emissivity will increase, causing a decrease in temperature. However, as the DBR reflectance spike matures, the significant contributions to ε_{tot} experience a relatively flat oscillitory waveform that adds one period for each added stack. The high-reflectance changes saturate at 900 nm and are not weighted heavily in the ε_{tot} calculation in any case. The oscillations in the 0.06-1.25 eV region are further diminished by interference effects from averaging over all incidence angles.

The difference in temperature transients between the AlAs and GaAs structures is simply related to the use of materials whose optical constants differ from that of the substrate. The larger the difference in the optical constant spectrum, the greater the chance that the total hemispherical emissivity will be significantly different than the substrate wafer. The optimum DBR test structure is therefore one whose optical constants do not differ strongly from the substrate while still maintaining a broad range of reflectance values as the reflectance maximum is achieved.

Effect of Temperature Oscillations on the Determination of Gamma

The temperature plots from ε_{tot} calculations presented above indicate that DBR structures are expected to exhibit very flat average temperature profiles after an initial transient. They are thus good candidates for extracting the γ factor described in section 4.3 and Appendix F. However, the calculations do predict that real periodic temperature oscillations are present during the growth of these structures. The variations are expected to be small, on the order of 1°, but could possibly interfere with the determination of the γ factor and could be mis-interpreted as temperature overcompensation artifacts.

An analysis of the effects of the temperature variations on the γ factor extraction is straightforward. Eq. [1.14] may be used to calculate a simulated thermal emission signal using the DBR reflectance at 900 nm for R, and solutions of the quartic surface temperature formula in Appendix A may be used as values for T. This correctly accounts for the combination of interference oscillations at 900 nm and the temperature oscillations from changes in total emissivity. To this synthesized signal may be added a constant offset representing γ factor effects and a ζ factor term. A specific example with $\tilde{\gamma} = 0.1$ and $\zeta = 0.05$ was chosen. Using synthesized thermal emission and reflectance signals, the minimum-variance method outlined in Appendix F was applied to the segment of data in the post-transient region ($t > 1000$ s). This yielded the correct value of $\gamma = 0.1579$ that would be obtained under absolutely constant temperature conditions. Because only a constant γ is being fit, the minimum-variation method effectively treats the real temperature oscillations simply as noise. The oscillations are symmetrically distributed about the mean temperature, so no bias in γ occurred. When the extracted value of γ was used in both the calibration expression for τ and the expression for T, Eq. [4.3], the original temperature waveform from the ε_{tot} calculation was extracted with no errors. The presence of real temperature oscillations is therefore not expected to interfere with the determination of the γ factor for eliminating temperature overcompensation effects. Residual oscillations after γ correction may indeed be real.

INITIAL DISTRIBUTION

1126 R. Biefeld
1126 W. Breiland (2)
1126 J. Creighton(5)

1	MS 9018	Central Technical Files, 8945-1
2	0899	Technical Library, 9616
1	0612	Review and Approval Desk, 9612

Prof. Martha Gallivan
School of Chemical Engineering
Georgia Institute of Technology
311 Ferst Dr./0100
Atlanta, GA 30332

Prof. Ian Ferguson
School of Electrical and Computer Engineering
Georgia Institute of Technology
Atlanta, GA 30332-0250